Three-Dimensional Shockwave/Boundary-Layer Interactions on Swept Compression Ramps at Mach 4

A Thesis Presented for the

Master of Science

Degree

The University of Tennessee, Knoxville

Jamison Murphree

August 2024

Approved for Public Release; Distribution Unlimited. Case Number

AFRL-2024-5997; Cleared 10/25/2024.

© by Jamison Murphree, 2024
All Rights Reserved.

Approved for Public Release; Distribution Unlimited. Case Number AFRL-2024-5997; Cleared 10/25/2024.

I dedicate this work to my parents, James and Megan, without whom none of this would be possible, and to my beautiful wife, Jill, for her unwavering love and support.

Approved for Public Release; Distribution Unlimited. Case Number AFRL-2024-5997; Cleared 10/25/2024.

Acknowledgments

I would like to thank my advisor, Dr. Phil Kreth, for his guidance and support both personally and academically. Whether it be his assistance during the long hours of code writing and data analysis, availability for help during the day or late into the evening, or his friendly practical jokes, his commitment to his students is unmatched. I would also like to thank Dr. John Schmisseur for allowing me the opportunity to intern at UTSI with the HORIZON group and for all of his sage wisdom and advice imparted to me throughout my undergraduate degree, internship, and my first year of graduate school. He is truly a mentor and someone I greatly admire.

I would also like to thank my other committee members: Dr. Trevor Moeller and Dr. Cary Smith for their guidance and feedback throughout this process. To John Strike, Kirk Davenport, and the research support staff: thank you for the assistance and willingness to teach valuable, practical engineering skills along every step of the way. To my fellow students at UTSI: thank you for always being there to help in the labs, study together, and for the good times we have had during our academic careers. Finally, I would like to thank the Air Force Research Laboratory for the funding of this work under contract number FA8650-20-C-2407.

Approved for Public Release; Distribution Unlimited. Case Number AFRL-2024-5997; Cleared 10/25/2024.

Abstract

Two-dimensional and three-dimensional shockwave/boundary-layer interaction (SBLI) dynamics are investigated using surface measurements on compression ramps in the University of Tennessee Space Institute's Mach 4 Ludwieg Tube. The experiments in the present work are building upon prior experiments conducted in a smaller facility at Mach 2 conditions. The goal of the current experiment was to conduct a "scale-up" exercise to investigate the effects of Mach number, Reynolds number, and other pertinent flow conditions on the dynamics of 2D and 3D SBLIs. The three model configurations consisted of a high sweep ramp ($\lambda = 27.5°$), a low sweep ramp ($\lambda = 10°$), and an unswept ramp ($\lambda = 0°$). All three ramps had a compression angle of 30°. Oil flow visualization, pressure sensitive paint, and pressure transducers were used to gather information on the separation shock location, separation region shape, and unsteadiness within the separation region.

The unswept ramp was not able to be analyzed due to loss of data via hard drive failure and damage that occurred to the model during the second pressure sensitive paint campaign. The low sweep and high sweep ramp data were able to be reduced and analyzed. The low and high sweep ramps exhibited cylindrical and quasi-conical symmetry, respectively (as anticipated). Other key findings included that the low sweep cases had greater unsteadiness globally compared to the high sweep case. In addition, the reattachment region had pressure fluctuations three times greater than the pressure fluctuations in the separation region for both sweep angles. The motion of the separation shock foot was normally distributed in both sweep cases, with dominant frequencies ranging from 200–400 Hz (for the low sweep case) and 700–800 Hz (for the high sweep case). Non-dimensionalizing these frequencies using the intermittent length as the characteristic length scale yielded Strouhal numbers in the range of $0.02 \leq St_L \leq 0.05$.

Approved for Public Release; Distribution Unlimited. Case Number AFRL-2024-5997; Cleared 10/25/2024.

Table of Contents

1 Introduction **1**

1.1 Motivation 1

1.2 Overview 2

1.3 Research Objectives 5

2 Methodology **9**

2.1 Experimental Methodology 9

2.1.1 Wind Tunnel Facility 9

2.1.2 Wind Tunnel Models 11

2.1.3 Oil Flow Visualization 13

2.1.4 Pressure Transducers 14

2.1.5 Pressure Sensitive Paint 17

2.1.6 Molecular Tagging Velocimetry 25

2.2 Analytical Methodology 26

2.2.1 Oil Flow Visualization 26

2.2.2 Pressure Transducers 27

2.2.3 Pressure Sensitive Paint 27

2.3 Uncertainty Analysis 28

2.3.1 Pressure Transducers 28

2.3.2 Pressure Sensitive Paint 29

3 Results and Analysis **33**

3.1 Oil Flow Visualization 33

3.2 Pressure Sensitive Paint 34

Approved for Public Release; Distribution Unlimited. Case Number AFRL-2024-5997; Cleared 10/25/2024.

4 Conclusions and Future Work **49**

4.1 Conclusions 49

4.2 Future Work 50

Bibliography **52**

Appendix **60**

A Use of Figures from Published Works 60

A.1 Figure 1.1 60

A.2 Figure 2.5 60

Vita **61**

Approved for Public Release; Distribution Unlimited. Case Number AFRL-2024-5997; Cleared 10/25/2024.

List of Figures

1.1 Schematic of cylindrical and conical symmetry in swept compression ramp flows. Reproduced from Settles and Teng [55] with permission. 7
1.2 Parameter space for existing swept ramp turbulent SBLI research. The asterisk shaped markers denote the present experiment. 8

2.1 Schematic of the UTSI Mach 4 Ludwieg Tube and ancillary equipment [33] . 10
2.2 3D-resin-printed compression ramps with varying sweep angles. Note that 2.2b shows the 10° sweep ramp with pressure sensitive paint applied to the ramp face. 12
2.3 Top-down view of the 27.5° swept ramp immediately following the end of a tunnel run. 15
2.4 Schematic of the floor plate, ramp, and Kulite locations. 16
2.5 Schematic showing the excitation and emission of luminophores for polymer-ceramic PSP. Reproduced from Gregory [23] with permission. 19
2.6 Possible energy state paths for excited luminescent molecules to return to the ground state. Adapted from Kavandi [27] 20
2.7 Photograph of the experimental setup for the compression ramp PSP campaign. 24

3.1 Oil flow visualizations on the two swept compression ramps. The approximate location of the Virtual Conical Origin (VCO) is identified on the highly swept case. 35
3.2 Average surface pressure distribution obtained over 2400 frames from the steady-state conditions run for both swept ramps. 36
3.3 P'_{RMS} (pressure fluctuation) contours obtained over 2400 frames from the steady-state conditions run for both swept ramps. 37

Approved for Public Release; Distribution Unlimited. Case Number AFRL-2024-5997; Cleared 10/25/2024.

3.4 P'_{RMS} contours superimposed onto oil flow visualization images for both swept ramps. 39
3.5 Example time history, cross correlation, and coherence of the PSP virtual tap and the Kulite within the separation region for the $\lambda = 10°$ sweep case. . . . 40
3.6 Example time history, cross correlation, and coherence of the PSP virtual tap and the Kulite within the separation region for the $\lambda = 27.5°$ sweep case. . . 41
3.7 Traces of P'_{RMS} extracted along $z/\delta_{99} = 0.05$ for both ramps. The large spikes are a result of discontinuities in the paint at the ramp-floor interface and damage to the surface by diaphragm particles. 45
3.8 Comparison of highly-swept ramp interactions from the current experiment and results from Erengil and Dolling [12]. 46
3.9 Probability density functions of the separation shock movement extracted from the PSP images for both ramps. The black lines represent a Gaussian distribution. 47
3.10 Pre-multiplied power spectral densities of the separation shock foot motion for both ramps. Zero-crossing frequencies and Strouhal numbers based on boundary layer thickness and intermittent length scale are shown. 48

Approved for Public Release; Distribution Unlimited. Case Number AFRL-2024-5997; Cleared 10/25/2024.

Nomenclature

Abbreviations

CFD Computational Fluid Dynamics

FLEET Femtosecond Laser Electronic Excitation Tagging

FOV Field of View

KTV Krypton Tagging Velocimetry

LED Light Emitting Diode

MTV Molecular Tagging Velocimetry

PDF Probability Density Function

PIV Particle Image Velocimetry

PLS Planar Laser Scattering

PSD Power Spectral Density

PSP Pressure Sensitive Paint

SBLI Shockwave/Boundary-Layer Interaction

SLBLI Shockwave/Laminar Boundary-Layer Interaction

STBLI Shockwave/Turbulent Boundary-Layer Interaction

TALon Tennessee Aerothermodynamics Laboratory

UTSI University of Tennessee Space Institute

UV Ultraviolet

Approved for Public Release; Distribution Unlimited. Case Number AFRL-2024-5997; Cleared 10/25/2024.

VCO Virtual Conical Origin

XSBLI Shockwave/Transitional Boundary-Layer Interaction

Greek

δ Boundary layer thickness

λ Sweep angle of the ramp face

Superscripts

$\acute{}$ Fluctuation from the mean value

Latin

$A_n(T)$ Stern-Volmer coefficents (temperature dependent)

I Intensity of fluorescence

L Intermittent length scale (length over which the separation shock traverses)

n Index of summation

p Pressure

St Strouhal Number

x Streamwise coordinate relative to the wind tunnel facility

z Spanwise coordinate relative to the wind tunnel facility

Subscripts

99 denotes the given variable as 99% of the freestream value

REF denotes the given variable as a reference condition

Approved for Public Release; Distribution Unlimited. Case Number AFRL-2024-5997; Cleared 10/25/2024.

Chapter 1

Introduction

1.1 Motivation

Shockwave/boundary-layer interactions (SBLIs) have been a topic of study within the aerospace community since the mid-twentieth century. SBLIs are known to cause a myriad of undesirable effects on aerospace vehicles. Some examples of these deleterious effects include unsteady pressure loads, increased heating, increased drag, and possible loss of control authority. Each of these effects can be detrimental to a flight vehicle [9]. This is evidenced by the infamous NASA X-15-2 incident where a pylon holding a dummy ramjet engine failed due to thermal and mechanical loading induced by shock-shock and shockwave/boundary-layer interactions despite having an ablative coating [64]. As a result, there has been strong interest in improving numerical modeling capabilities and obtaining a better understanding of the dynamics of SBLIs from experimental and numerical studies in order to control and/or mitigate these effects.

One of the primary considerations among much of the past research into SBLIs has been the state of the incoming boundary layer. The variations found in the literature are named as follows: shockwave/laminar boundary-layer interaction (SLBLI), shockwave/transitional boundary-layer interaction (XSBLI), and shockwave/turbulent boundary-layer interaction (STBLI). Laminar boundary layers and interactions can be predicted reasonably well with computational fluid dynamics (CFD) solvers [15]. Historically, CFD has struggled to accurately predict the dynamics of strong transitional and turbulent boundary-layer interactions, particularly in regards to the surface pressures, heat transfer, and primary

Approved for Public Release; Distribution Unlimited. Case Number AFRL-2024-5997; Cleared 10/25/2024.

separation location [30]. Consequentially, many experimental investigations tend to focus on these two types of SBLIs.

In addition to their characterization based upon the incoming boundary-layer state, SBLIs are also categorized as having two-dimensional (2D) or three-dimensional (3D) interactions. The distinction between 2D and 3D is determined by the model geometry, typically from the extent of the spanwise variation in the interaction. Well-known reviews on several canonical geometries and the associated SBLI dynamics are available from Clemens and Narayanaswamy [7] as well as Gaitonde and Adler [16]. The former focuses on closed interactions (i.e., typically 2D) and the latter focuses on open interactions (i.e., 3D), although there is significant crossover between the two in discussing the nuances of both types of interactions.

1.2 Overview

Compression ramps are commonly used as the shock-generating geometry in both 2D and 3D SBLI studies because they have large variations in spanwise flow relief that are dependent upon the sweep angle of the ramp face. Normally, a compression ramp would generate a 2D interaction, whereas a swept compression ramp would generate a 3D interaction as the ramp geometry varies in the spanwise direction and allows the flow to follow the sweep angle of the ramp face. This brings about another important consideration for SBLI dynamics: the nature of the separation region (e.g., whether it exists in a closed or open form). If the separation region is closed, then the separated fluid is effectively trapped and mostly all of the fluid in this region continuously recirculates. An unswept compression ramp produces a closed interaction. In contrast, if the separation region is open, the separated flow can move downstream. A swept compression ramp produces an open interaction, but the shape of the separation region can change depending on the sweep angle (primarily).

Settles and Teng [55] observed this phenomenon and defined swept interactions based on the shape of the separation region. If the separation and reattachment shocks are approximately parallel, they define that interaction as exhibiting cylindrical symmetry. On the other hand, if the separation and reattachment shocks diverge from one another in the

Approved for Public Release; Distribution Unlimited. Case Number AFRL-2024-5997; Cleared 10/25/2024.

spanwise direction but with constant angles with respect to the incoming flow direction, they define that interaction as having conical symmetry. Low sweep compression ramps typically produce interactions with cylindrical symmetry; however, as the sweep angle increases, the separation region begins to exhibit a conical shape. Settles and Teng [55] created schematics of these interactions as shown in Fig. 1.1. For conically symmetric separation regions, it is useful to specify the geometry by defining a singular point or origin from which the conical shape can be traced. This location was originally defined by Settles and Teng [55] as the intersection point of lines tracing the upstream influence, separation shock, and reattachment shock. They called this intersection point the Virtual Conical Origin (VCO). They also noticed that the interactions were neither cylindrical or conical in nature close to the apex of the ramps due to the curvature of the separation and reattachment shocks. For this reason, they began to refer to the symmetry as "quasi"-conical. The region where the separation and reattachment shocks were curved was defined as the inception zone, denoted as L_i in Fig. 1.1, which is the length along the ramp face required for the flow to fully establish either cylindrical or conical symmetry. L_{mi} denoted the length from the reattachment shock to the upstream influence.

Over the past forty-five years, there have been several experiments conducted on swept compression ramps in supersonic flows. As discussed earlier, Settles and Teng [55] first defined the cylindrical and quasi-conical symmetry seen in swept compression ramp flows. Several other key investigations on swept compression ramps have been summarized in the following paragraphs.

Erengil and Dolling [12] conducted a study focusing on the effects of sweep angle on compression ramps at Mach 5. The compression angle of their ramps were 28 degrees and the sweep angles they used were 0, 10, 20, 25, 30, 40, and 50 degrees. They found that ramps with sweep angles less than 25 degrees were cylindrically symmetric, whereas ramps with sweeps greater than or equal to 25 degrees exhibited quasi-conical symmetry. They also found that as the sweep angle increases, the pressure fluctuations decreased within the observable interaction region. The length of the intermittent region decreased with increasing sweep, resulting in higher frequencies of shock foot translation. The frequencies of the dominant

Approved for Public Release; Distribution Unlimited. Case Number AFRL-2024-5997; Cleared 10/25/2024.

separation shock foot motion ranged from 0.3–0.5 kHz for unswept flows and 2–7 kHz for highly swept flows.

Vanstone *et al.* [59]–[63] conducted a series of experiments over the course of several years on a swept ramp at Mach 2 with a compression angle of 22.5 degrees and a sweep angle of 30 degrees. Their first set of experiments consisted of oil flow visualization and Particle Image Velocimetry (PIV) [61]. The oil flow revealed the expected quasi-conical symmetry of the separation and reattachment lines. Further investigation of the separation region showed reduced streamwise velocities, although reversed flow was only present close to the ramp face. Strong cross flow velocities (spanwise along the width of the ramp face) were observed in the separation region.

The second set of experiments utilized PIV and Planar Laser Scattering (PLS) to continue to observe flow structure and unsteadiness on the same ramp geometry [62]. They found that the instantaneous separation line was correlated to streamwise fluctuations in the incoming boundary layer, and that the bulk motion of the separation line appeared to be affected by the momentum of the incoming boundary layer. Although, they did acknowledge that additional sources of unsteadiness may be still be present.

In 2018, Vanstone *et al.* [63] detailed their findings for swept ramps with identical sweep but differing compression angles at Mach 2 using PIV and oil flow visualization. One ramp had a compression angle of 19 degrees and the other had a compression angle of 22.5 degrees. Both ramps had sweep angles of 30 degrees. They showed that both ramps exhibited quasi-conical behavior, as expected, given the large sweep angle. They found that the bulk flow features, such as the upstream influence, separation shock, and reattachment shock, exhibited quasi-conical behavior. The streamwise velocity fields showed similar quasi-conical behavior, but the velocities within the region of separated flow did not. They hypothesized that the separation region was highly sensitive to how the flow originated. This implied that the inception length was not uniform for every swept SBLI, but rather it seemed to depend on strength of the interaction. This thought process led them to believe that swept interactions traditionally coined as cylindrically symmetric may actually be more appropriately deemed very weakly quasi-conically symmetric.

Approved for Public Release; Distribution Unlimited. Case Number AFRL-2024-5997; Cleared 10/25/2024.

Allen *et al.* [2] conducted a study on swept compression ramps at Mach 2. They found that for their highly swept ramp ($\lambda = 30°$), the average separation location was approximately $1.9\delta_{99}$ upstream of the ramp centerline, and the dominant frequencies of the unsteady pressure fields associated with this region ranged between 0.7 and 2.2 kHz. The average separation location of their low sweep ramp ($\lambda = 10°$) was approximately $1.14\delta_{99}$ upstream of the ramp centerline and the dominant frequencies were about 0.7 kHz. In both cases, the pressure fluctuations within the separation region had elevated content at frequencies ranging from 8–15 kHz.

1.3 Research Objectives

Figure 1.2 shows the parameter space of compression ramp SBLIs in terms of Mach number and sweep angle. Here, available literature has been referenced and the configurations from the present study are included. Currently, there are limited experimental investigations of turbulent SBLIs generated by swept ramps, and to the author's knowledge, there are no results published for turbulent SBLI experiments on swept ramps subjected to Mach 4 flow (i.e., the present conditions). The goal of this work is to "scale up" from the prior work conducted by Allen *et al.* [2] to see how the increase in physical scale, Mach number, and Reynolds number affect the SBLIs on similar swept compression ramps. In addition, this work will help fill the gap in turbulent swept ramp SBLI research at Mach 4. The following goals for this work are outlined:

1. *Fill critical research gaps for turbulent SBLIs on swept compression ramps at Mach 4*

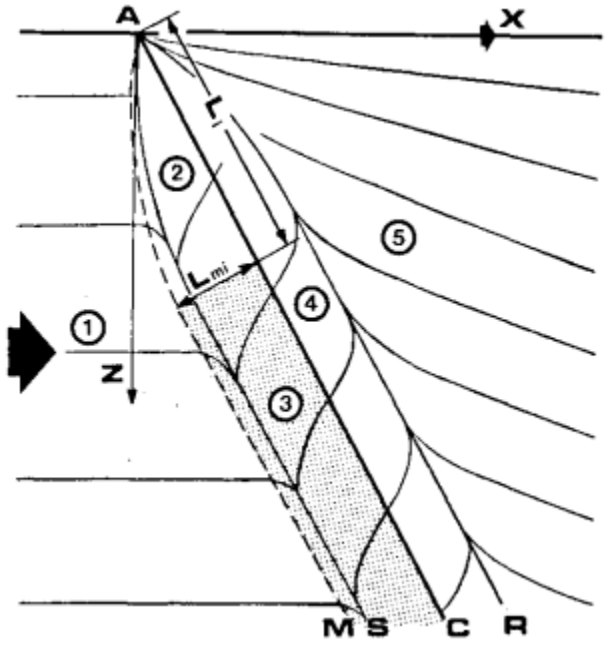
   The results of this experiment will provide data points to the existing research space on swept compression ramps. Additionally, the large size of the Ludwieg Tube used for the experiments also allows these experiments to have larger models and boundary-layer thicknesses than any previous swept compression ramp research.

2. *Determine which aspects (if any) of the separation region unsteadiness can be related to known parameters, such as physical scale, Mach number, Reynolds number, boundary-layer thickness, etc.*

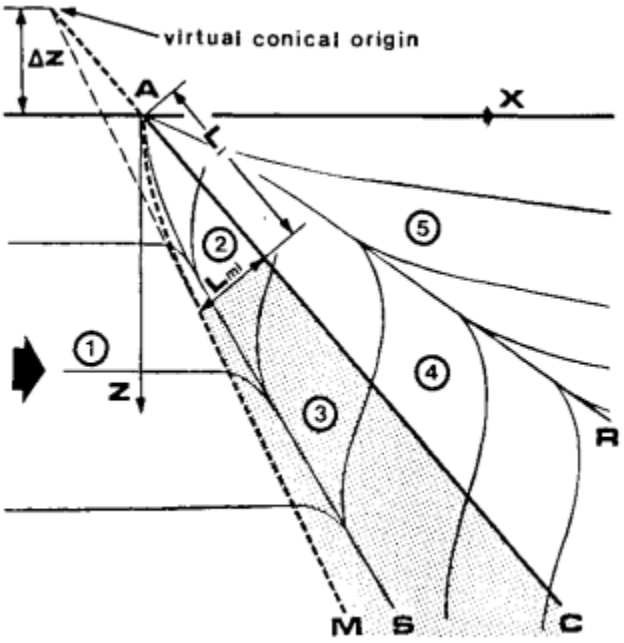
Approved for Public Release; Distribution Unlimited. Case Number AFRL-2024-5997; Cleared 10/25/2024.

The results produced from this experiment will be compared to the work of Allen *et al.* [2] as a part of a direct "scale-up" exercise. Additionally, results from existing swept compression ramp literature will be used for comparison of the parameters listed above. Location, magnitude, and characteristic frequency of separation region unsteadiness are critical for determining increased thermal/mechanical loading and control authority of a flight vehicle.

Approved for Public Release; Distribution Unlimited. Case Number AFRL-2024-5997; Cleared 10/25/2024.



(a) Cylindrically symmetric interaction



(b) Conically symmetric interaction

Figure 1.1: Schematic of cylindrical and conical symmetry in swept compression ramp flows. Reproduced from Settles and Teng [55] with permission.

Approved for Public Release; Distribution Unlimited. Case Number AFRL-2024-5997; Cleared 10/25/2024.

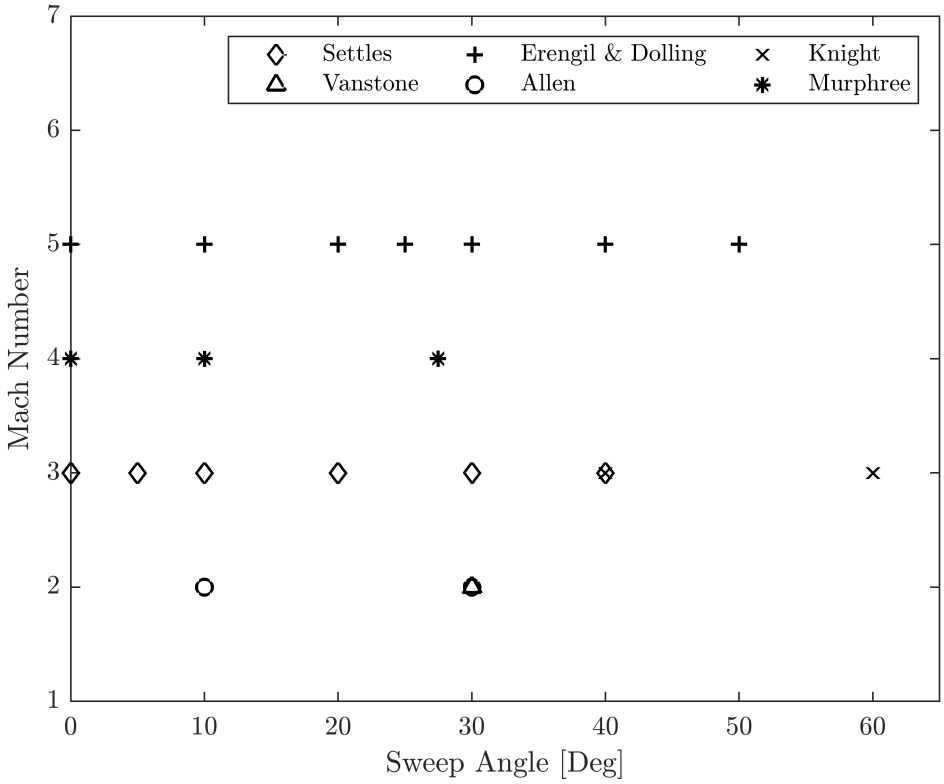


Figure 1.2: Parameter space for existing swept ramp turbulent SBLI research. The asterisk shaped markers denote the present experiment.

Approved for Public Release; Distribution Unlimited. Case Number AFRL-2024-5997; Cleared 10/25/2024.

Chapter 2

Methodology

2.1 Experimental Methodology

2.1.1 Wind Tunnel Facility

The Tennessee Aerothermodynamics Laboratory (TALon) at the University of Tennessee Space Institute (UTSI) houses a large scale Mach 4 Ludwieg Tube. It operates by pressurizing a long section of pipe, called the driver tube, until one or more stacked Mylar® diaphragms burst and allow the pressurized air to flow downstream through a 2D nozzle into the test section and subsequently into a vacuum tank. Diaphragms can be stacked to vary the unit Reynolds number over a range spanning from 1-16 $\times 10^6$ /ft (3.3-53 $\times 10^6$ /m). The facility generates steady-state Mach 4 flow in the 24" $\times$ 24" $\times$ 72" test section for approximately 105-120 ms per run. The test section has two large windows (11" $\times$ 17") for optical access. The turbulent boundary layer on the tunnel floor has a thickness of approximately 2.5" ($\delta_{99} \sim 2.5$"). Figure 2.1 shows an illustration of the Mach 4 facility from Kreth *et al.* [33]. Note that the expansion joint connecting the driver tube to the nozzle experienced a failure and is no longer implemented in the current operating state of the Mach 4 tunnel. The tunnel was redesigned for the driver tube to mate directly to the nozzle block. This does not affect the operating conditions of the facility.

Approved for Public Release; Distribution Unlimited. Case Number AFRL-2024-5997; Cleared 10/25/2024.

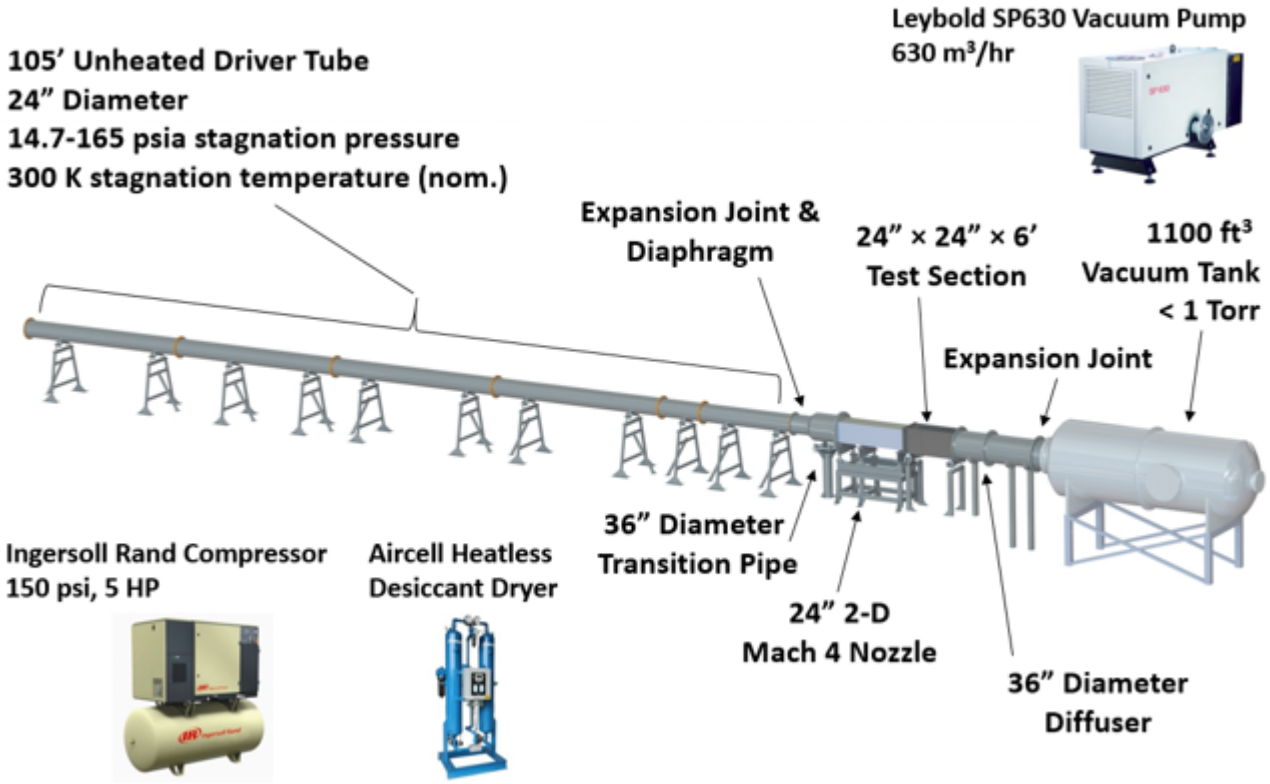


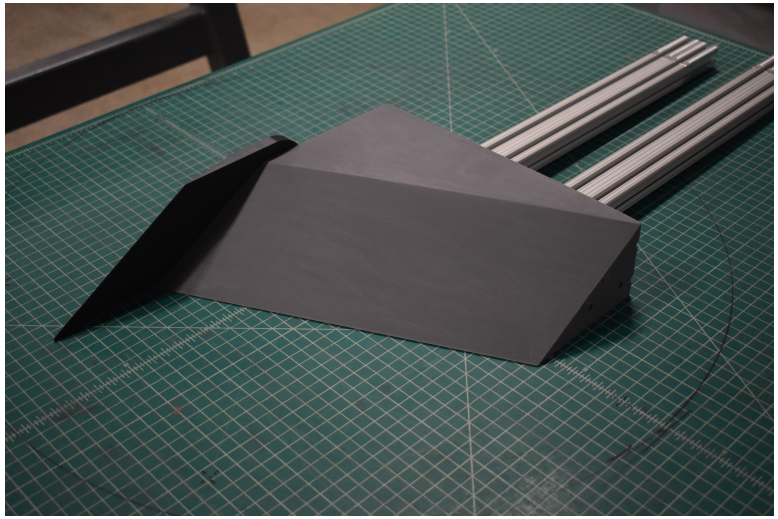
Figure 2.1: Schematic of the UTSI Mach 4 Ludwieg Tube and ancillary equipment [33]

Data shown in the current work are obtained at tunnel operating conditions using two stacked diaphragms, which results in a nominal burst pressure of 50 psia (345 kPa). The stagnation pressure realized after the rupture is approximately 90% of this burst pressure, which corresponds to 45 psia (310 kPa). Using this stagnation pressure value with the pressure ratio obtained from the isentropic flow relations (at Mach 4), the nominal test-section static pressure was 0.3 psia (2.1 kPa), and pressure transducers in the tunnel floor show a mean pressure during steady-state of 0.3 psia (2.1 kPa). The unit Reynolds number achieved at these conditions is approximately 4.4 $\times 10^6$ /ft (14.4 $\times 10^6$ /m).

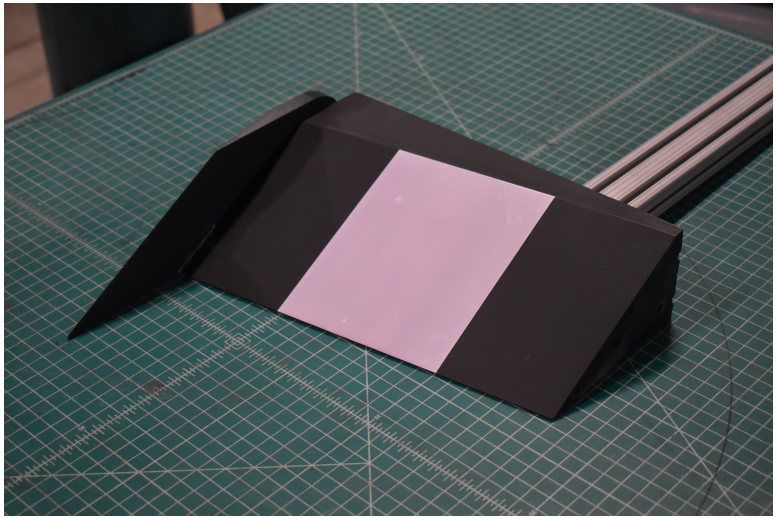
2.1.2 Wind Tunnel Models

The compression ramp models used for these experiments are shown in Figure 2.2. All three compression ramps have a span of 12", height of 3", and a compression angle of 30°. The 30° compression angle was selected based upon the Korkegi criterion for 2D incipient separation [32] and compressible flow theory. The Korkegi criterion at Mach 4 indicates a minimum angle of 21.7° compression for separation to occur, while the oblique shock relations limit the compression angle to a maximum of 38.7° for the shock to remain attached to the ramp corner. A 30° compression angle falls firmly between these upper and lower limits and ensured separation of the flow without detachment of the shock. Sweep angles of 27.5° and 10° were chosen to produce open and closed interactions, respectively. An aerodynamic fence attaches to both of the swept ramps to prevent spillage of flow over the apex side and to isolate the interaction. The fence extends 4 inches ($1.6\delta_{99}$) past the apex of the ramps. All of the models were painted matte black to provide contrast with the fluorescent dye for oil flow visualization and to reduce laser reflections for future molecular tagging velocimetry experiments.

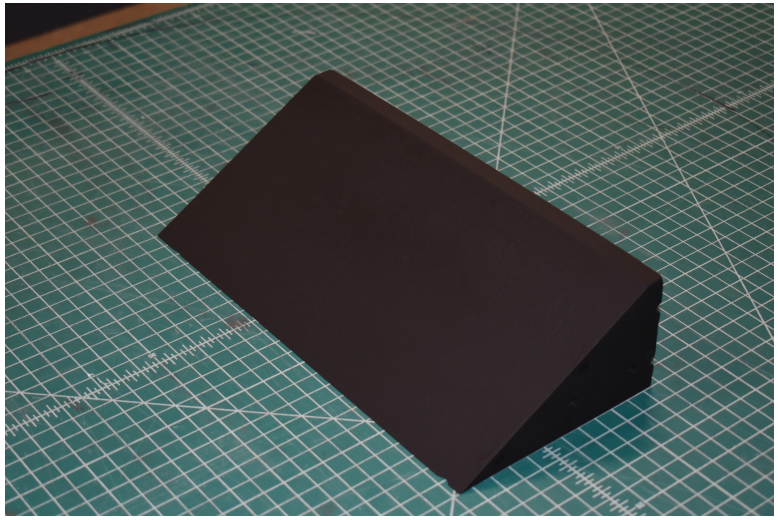
Approved for Public Release; Distribution Unlimited. Case Number AFRL-2024-5997; Cleared 10/25/2024.



(a) 27.5° Sweep



(b) 10° Sweep



(c) 0° Sweep

Figure 2.2: 3D-resin-printed compression ramps with varying sweep angles. Note that 2.2b shows the 10° sweep ramp with pressure sensitive paint applied to the ramp face.

Approved for Public Release; Distribution Unlimited. Case Number AFRL-2024-5997; Cleared 10/25/2024.

2.1.3 Oil Flow Visualization

Oil flow visualization has been utilized by aerodynamicists in wind tunnel testing for many decades. It is extremely useful in identifying key flow features. Oil flow is largely a qualitative diagnostic. However, once key flow features have been identified, further measurement techniques can be employed to collect quantitative data in the regions of interest. Traditionally, oil flow was conducted using lamp black pigment or titanium dioxide as dyes mixed with an oil. This mixture was spread on a surface just upstream of an area of interest. As the flow moved over the surface, it "dragged" the oil along with it. This process left streaklines that allowed experimentalists to visualize how the flow interacts with the model surface. Lu [37] provides a helpful history and overview of surface oil flow visualization. In the past, experimentalists would observe the streaklines and take photographs of them after the tests had concluded. More recently, the maturation of high-speed photography has allowed for hundreds to thousands of frames to be captured per second. This means that experimentalists can observe the formation of the streaklines and choose frames where the streaklines are fully-developed but not yet disturbed by tunnel unstart or wave passages. Additionally, the choice for dyes has largely shifted to fluorescent pigments. These pigments are excited by ultra-violet (UV) light and their fluorescence can be captured by high-speed cameras.

For the present experiment, oil flow visualization experiments were conducted to highlight key features of the flowfield (e. g. , the separation and reattachment regions) induced by the ramp geometries. Given the short run time of the Ludwieg tube utilized for this experiment, it was challenging to produce the necessary streaklines to reveal the flow patterns. An oil with low viscosity was required to produce enough movement to visualize the streaklines. In addition, a high-speed, triggerable camera was required to capture images during the steady-state portion of the tunnel run.

Eagan *et al.* [11] had success conducting oil flow experiments on a Busemann Inlet in the UTSI Mach 4 Ludwieg Tube. As a result, their mixture was used in the present experiments. The oil used was polydimethylsiloxane with a viscosity of 5 cSt and the pigment was Smooth-On Silc Pig fluorescent silicone pigment. They recommended an oil to pigment mixture ratio

Approved for Public Release; Distribution Unlimited. Case Number AFRL-2024-5997; Cleared 10/25/2024.

of approximately 12:1 by volume. The oil mixture was applied in a loose grid pattern of large circles using a pipette. Each circle contained approximately 700 μL of the oil mixture. Once applied, the oil was exposed to ultraviolet light produced by two UV LEDs. These were high-intensity, water-cooled LEDs (manufactured by Innovative Scientific Solutions, Inc.) and produce UV light at a wavelength of 400 nm. When excited by the UV light, the oil mixture fluoresced, and its emission was captured using a Photron FASTCAM Mini AX200.

The camera acquisition rate was set to 5000 frames per second in order to capture the most amount of frames while maintaining full field of view of the ramp. A 450 nm longpass filter was used to block out the excitation wavelengths from the UV LEDs. A photo from the end of an oil flow experiment is shown in Fig. 2.3. Note the streaklines following the spanwise relief of the ramp and the reattachment shock on the ramp face. This image provides a good view of oil flow in general, however, due to the rebounding expansion wave and tunnel motion the oil can move after the steady-state portion of the tunnel run. For this reason, instantaneous images during the tunnel run are used for analysis.

2.1.4 Pressure Transducers

Two Kulite pressure transducers (model numbers XCE-080 and XCE-062) were used in the floor plate directly upstream of the ramp models for discrete pressure measurements. One transducer was located 0.75" ($0.3\delta_{99}$) upstream of the ramp face, and the other was located 8" ($3.2\delta_{99}$) upstream of the ramp face. An illustration of the floor plate insert for the Mach 4 tunnel with embedded Kulite locations is shown in Figure 2.4. Both Kulites were sampled at 80 kHz and were calibrated at the same time as the PSP using the Druck DPI612 pressure calibration unit. The Kulites were connected to a KSC-2 signal conditioner that provided power to the transducers and conditioned their outputs which were amplified by an input gain of 8 and an output gain of 12.5. The KSC-2 filter cutoff frequency was set to 32 kHz. The amplified signal from the KSC-2 was input into a National Instruments (NI) PXIe-6358 data acquisition system (DAQ) held within an NI PXIe-1090 chassis.

Approved for Public Release; Distribution Unlimited. Case Number AFRL-2024-5997; Cleared 10/25/2024.

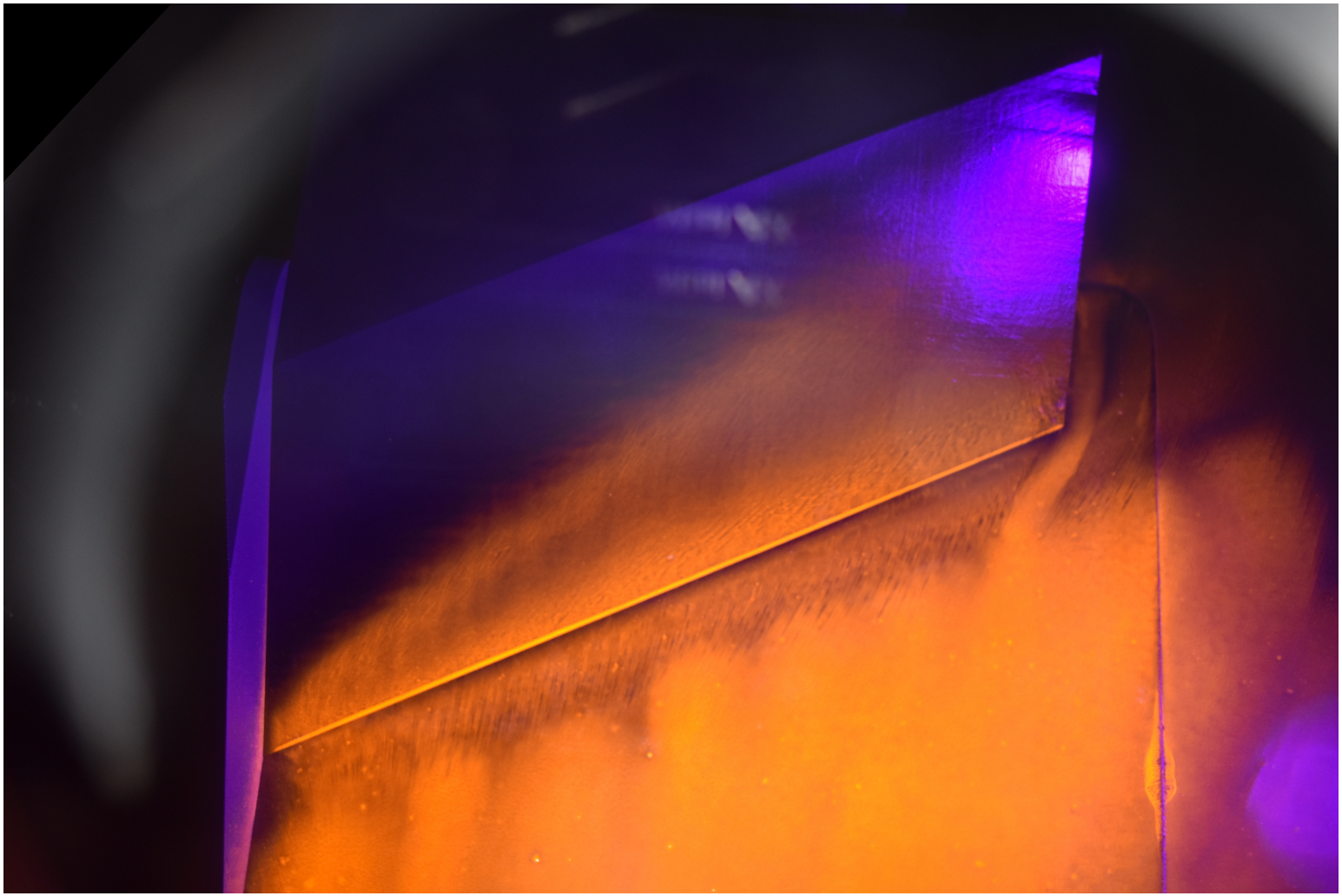


Figure 2.3: Top-down view of the 27.5° swept ramp immediately following the end of a tunnel run.

Approved for Public Release; Distribution Unlimited. Case Number AFRL-2024-5997; Cleared 10/25/2024.

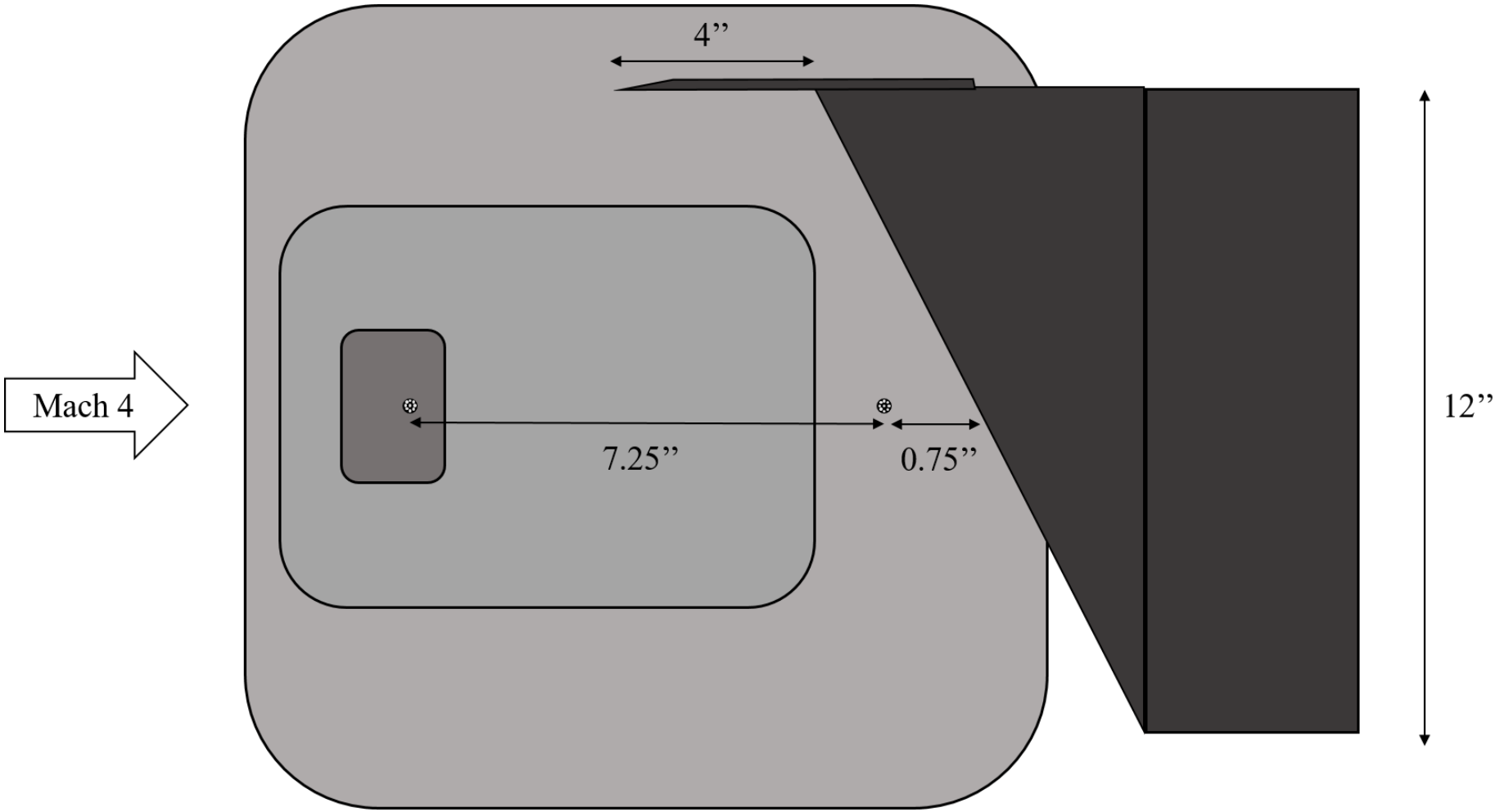


Figure 2.4: Schematic of the floor plate, ramp, and Kulite locations.

Approved for Public Release; Distribution Unlimited. Case Number AFRL-2024-5997; Cleared 10/25/2024.

2.1.5 Pressure Sensitive Paint

Pressure sensitive paint (PSP) is a recently developed diagnostic technique capable of measuring global surface pressures. This application can be incredibly useful in aerodynamic testing to obtain full-field pressure data when pressure transducers are not feasible. In general, PSP works by exciting luminescent particles (sometimes referred to as luminophores) within the paint using an ultra-violet light of appropriate wavelength. The wavelength required for excitation is dependent on the properties of the luminophores used in a particular PSP formulation. The luminophores fluoresce when exposed to UV light, and the intensity of the fluorescence is dependent on the local partial pressure of oxygen at those specific luminophore particles. Luminophores that interact with oxygen molecules experience "oxygen quenching". This is the process by which oxygen molecules interfere with the emission of photons by the luminophores. A higher partial pressure of oxygen results in more oxygen quenching and a lower intensity fluorescence by the luminophore. The luminescent intensity can be measured using a high-speed camera and processed to yield pressure fields in the painted areas of interest. When coupled with pressure transducers as anchor points, PSP can provide quantitative pressure values at each pixel of the acquired images [39].

One of the first instances of fluorescence being leveraged as a diagnostic technique was a demonstration of flow visualization via oxygen quenching of luminescent particles by Peterson and Fitzgerald [45]. This process was pioneered for aerodynamic testing by scientists in the Soviet Union throughout the 1980s and 1990s at the Central Aero-Hydrodynamic Institute (TsAGI), although their research was not well known until the 1990s. TsAGI partnered with an Italian company called INTECO to produce a PSP system that was demonstrated in wind tunnel facilities in the United States and Germany in the early 1990s [35, 36]. Similarly, pressure sensitive paints were developed by a research group at the University of Washington in the early 1990s [28]. The concepts and fundamental principles of PSP were later expounded upon by McLachlan and Bell at NASA Ames Research Center for use in further wind tunnel testing [39].

Approved for Public Release; Distribution Unlimited. Case Number AFRL-2024-5997; Cleared 10/25/2024.

As the flight regimes of interest increased in speed, continued investigations of the response times of paint formulations were required in order for PSP to remain useful as a high-speed diagnostic technique. Baron *et al.* [5] found that the diffusivity of the base coat material has significant effects on the response time of the paint. This led to the revelation that porous substrate materials can be utilized to push the response time of the paint into the sub-millisecond range. Ponomarev and Gouterman [47] were the first to discover that high concentrations of hard pigment particles created a porous substrate leading to a fast response paint formulation.

More recently, a company based in Dayton, Ohio called Innovative Scientific Solutions, Inc. (ISSI) has developed several proprietary PSP formulations. These formulations have primarily been fast response PSPs to accommodate the need for high-speed wind tunnel testing with the recent rise of hypersonic aerodynamics research. ISSI has partnered with several institutions to research high-speed aerodynamic phenomena [8, 66, 43]. ISSI currently offers their PSP formulations for sale for use in external research along with other ancillary devices, such as high-intensity light sources, calibration systems, and PSP starter kits.

Theory

The general theory behind pressure sensitive paints is that they take advantage of the oxygen-quenching properties of certain luminescent molecule in order - for the images of the fluorescence - to be extrapolated to pressure fields. To accomplish this, most PSPs consist of some form of base coat on the model as well as a top coat that carries and deposits the luminescent particles, also known as luminophores, onto the desired surface. Figure 2.5 shows a graphic that depicts the excitation and emission of luminophore molecules on a model surface.

Approved for Public Release; Distribution Unlimited. Case Number AFRL-2024-5997; Cleared 10/25/2024.

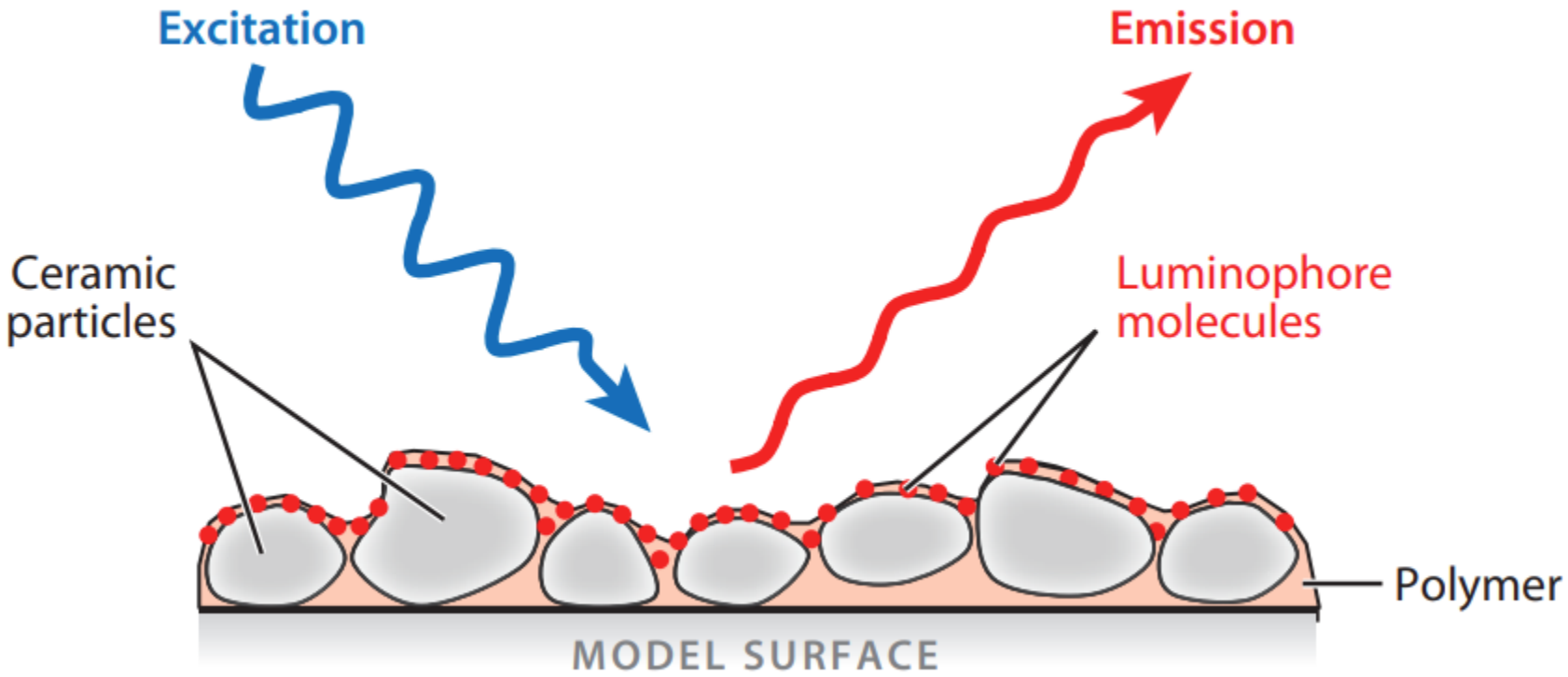


Figure 2.5: Schematic showing the excitation and emission of luminophores for polymer-ceramic PSP. Reproduced from Gregory [23] with permission.

Approved for Public Release; Distribution Unlimited. Case Number AFRL-2024-5997; Cleared 10/25/2024.

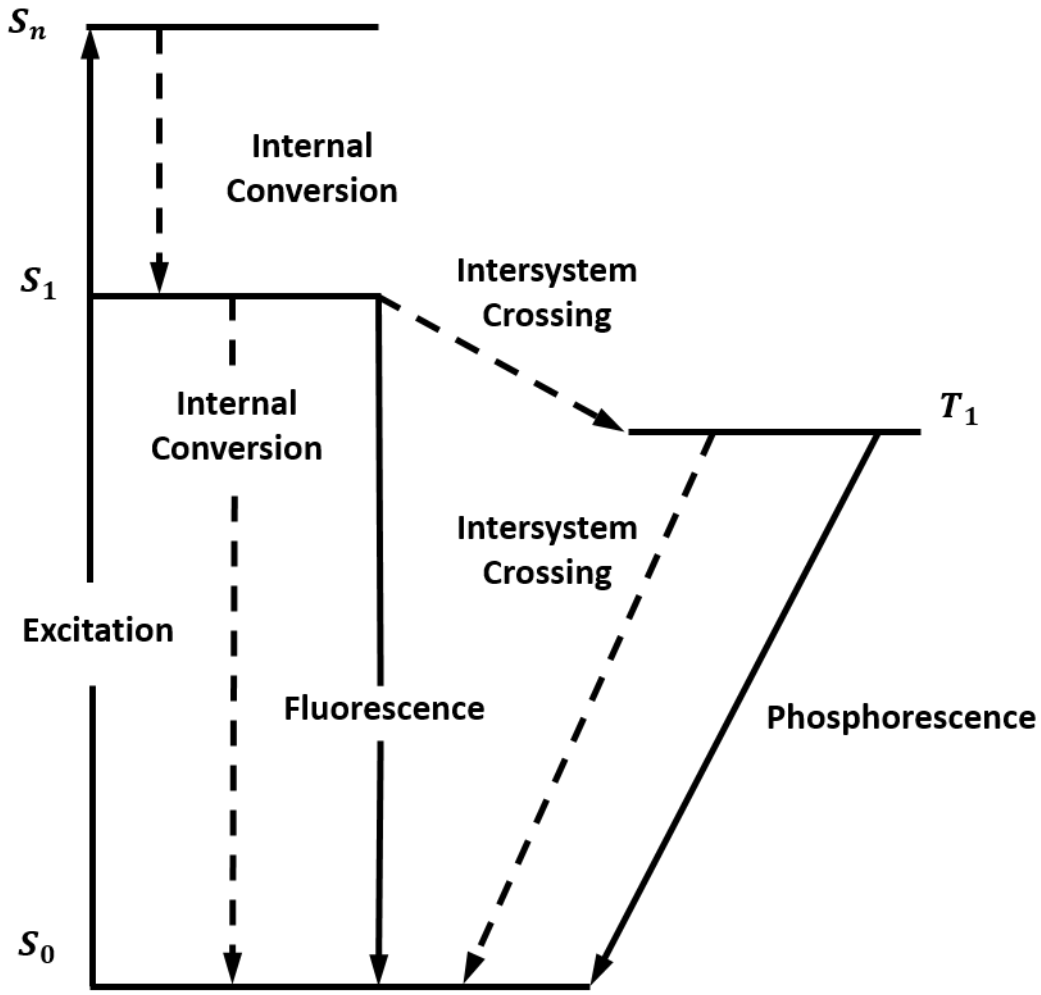


Figure 2.6: Possible energy state paths for excited luminescent molecules to return to the ground state. Adapted from Kavandi [27]

Approved for Public Release; Distribution Unlimited. Case Number AFRL-2024-5997; Cleared 10/25/2024.

The painted area of interest is exposed to a UV light source that excites the luminophores to an elevated energy state. This elevated energy state has a finite lifetime. Through several different processes, the excited luminescent molecules will return to the ground state. The first of these processes is the emission of photons, the second is the release of heat, and the third is a reaction with oxygen. The ground state of oxygen reacts with the excited luminescent molecules when they come into contact thereby reducing the overall emission intensity. This process is called oxygen quenching. Figure 2.6 shows energy conversion paths for the excited molecules.

An excited electron in the luminescent molecule can exist in a singlet state (S_i) or a triplet state (T_i), where i represents the energy level. In the singlet state, the electron has the same spin as the ground state electron. In the triplet state, the electron does not have the same spin as the ground state electron. Higher energy levels S_i ($i > 1$) decay to S_1 through an internal conversion process that converts vibrational energy to heat. From S_1, the electron may continue to decay to the ground state (S_0) by releasing heat or by emitting photons. The electron may also move to a triplet state (T_1) via a process called intersystem crossing. Eventually all higher energy level states must relax to the ground state. Emissions from S_1 to S_0 are called fluorescence. Emissions from T_1 to S_0 are called phosphorescence. Phosphorescence has longer lifetimes than fluorescence and both are classified as luminescence [36, 18].

Both fluorescence and phosphorescence are affected by the phenomenon of oxygen quenching. This means that more oxygen content in the air will result in greater quenching. Therefore, higher pressures in systems that use air or oxygen as a working gas result in increased oxygen content and lower luminescent intensities. The opposite also holds true: as pressure decreases the luminescent intensities increase. This inversely proportional relationship is described in a modified version of the Stern-Volmer relationship [36] shown in Eq. 2.1.

$$\frac{P}{P_{\mathrm{REF}}} = \sum_{n=0}^{N} A_n(T) \left(\frac{I_{\mathrm{REF}}}{I} \right)^n \tag{2.1}$$

Approved for Public Release; Distribution Unlimited. Case Number AFRL-2024-5997; Cleared 10/25/2024.

In Eq. 2.1, I are the intensity values of a given image, I_{REF} are the intensity values of an image at a known reference pressure, P_{REF} is the known reference pressure, and P are the desired pressure values. When the calibration coefficients, A_n, are known, it becomes trivial to convert a measured intensity value to a pressure value. For commercially available PSPs, these constants are typically provided by the manufacturer. For PSPs where these constants are not readily known, a calibration curve must be constructed. This can be done by stepping through a series of known pressures and measured intensity values. The intensity ratios can then be plotted against the pressure ratios and have a curve fit applied to them. The coefficients of the n^{th} order curve fit correspond to the A_n coefficients. It is important to note that these coefficients are temperature dependent. For the most accurate results, it is recommended to perform *in situ* calibrations by repeating the above process within the facility while taking special care to note the ambient temperature at time of calibration.

Recent Developments

Significant work has been done on developing and refining PSP technology for large scale wind tunnel testing by NASA Ames Research Center and the Arnold Engineering Development Complex. Research by Roozeboom *et al.* [50, 49] and Murakami *et al.* [41] have focused on the implementation of PSP in the NASA Ames Unitary Plan Wind Tunnel and data reduction processes. A notable example of their work at Ames is the use of PSP to measure fluctuating surface pressures for the pre-flight ground testing of the NASA Space Launch System.

Researchers at the University of Tennessee Space Institute have been experimenting with the use of PSP in both Ludwieg Tubes and blowdown facilities. Ledbetter *et al.* [34] used PSP to investigate the streamwise vortices on a hollow-cylinder/flare model using a Mach 4 Ludwieg Tube. They found that the frequency of the pressure fluctuations caused by the vortices were typically between 2-3 kHz. Butera *et al.* [6] attempted to use PSP to observe boundary layer transition on the BOLT II model geometry in the Mach 7 Ludwieg Tube, but ultimately found that the extremely low static density of that facility led to poor paint response. Allen *et al.* [2] performed PSP experiments on swept compression ramps with varying sweep angle in the Mach 2 blowdown facility. They found that the unsteadiness of

Approved for Public Release; Distribution Unlimited. Case Number AFRL-2024-5997; Cleared 10/25/2024.

the separation region pressure fluctuations increased to higher frequencies as the sweep angle of the ramp increased.

Current Experiment

For this experiment, Pressure Sensitive Paint (PSP) measurements were performed using ISSI's Porous, Fast-Response PSP formulation. This is a single luminophore formulation which has a purported response time less than 100 μs, and ISSI claim their paint can resolve frequencies greater than 10 kHz [1]. The base coat of the paint is an oxygen porous polymer-ceramic, and the top coat consists of luminescent, oxygen sensing particles. The base coat is applied to the models and allowed to dry overnight. The top coat is applied directly over the base coat. Both the base coat and top coat were applied using high volume, low pressure (HVLP) spray guns. The paint is replaced for each model configuration or if the paint is significantly damaged by pieces of the Mylar® diaphragms.

The excitation light for the PSP is provided by the same UV lamps used for the oil flow experiments. Parabolic reflectors were attached to the UV LEDs to focus the light onto the models. The PSP images were captured using a Photron FASTCAM SA-Z high-speed camera and were acquired at 20 kHz with an exposure time of 48.39 μs. A 50 mm f/1.4 Nikon lens is used in conjunction with a 450 nm and 610 nm longpass filter. The 450 nm longpass filter blocks the UV LEDs excitation wavelength and the 610 nm wavelength filter blocks any remaining wavelengths shorter than 610 nm. The PSP emission has a wavelength of 650 nm. This setup can be seen in Fig. 2.7. The ramps were mounted on the tunnel ceiling with the high-speed camera looking through a viewport on the floor of the tunnel. The excitation light was provided by UV LEDs through large windows installed in the sidewalls of the tunnel.

Approved for Public Release; Distribution Unlimited. Case Number AFRL-2024-5997; Cleared 10/25/2024.

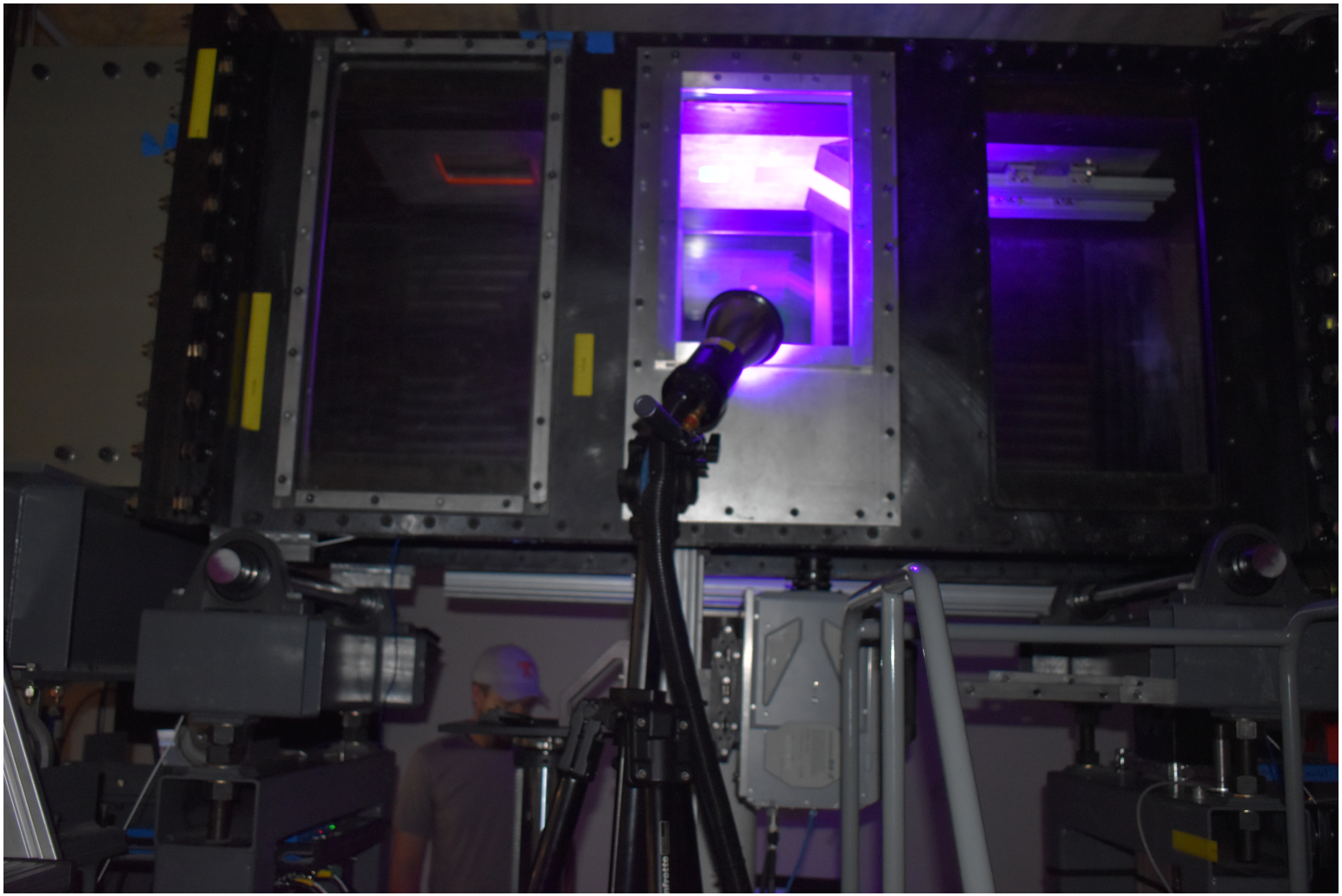


Figure 2.7: Photograph of the experimental setup for the compression ramp PSP campaign.

Approved for Public Release; Distribution Unlimited. Case Number AFRL-2024-5997; Cleared 10/25/2024.

An *in situ* static calibration was performed while vacuuming the test section during the standard tunnel operation procedures. A series of five points between 5 psia and 0.1 psia were measured using a Druck DPI612 pressure calibration unit as the reference pressure. Simultaneously, images were taken of the PSP so the reference intensities could be related to the reference pressures. The pressure ratios and intensity ratios were related with a second-order curve fit that provides the Stern-Volmer coefficients. These coefficients, as well as the reference pressure and intensity values, were used to convert the "wind on" image intensities to pressure using the Stern-Volmer relationship shown in Eq. 2.1. This process was repeated each time a new coat of paint was applied.

2.1.6 Molecular Tagging Velocimetry

Molecular Tagging Velocimetry (MTV) is an optical diagnostic technique used to measure the velocities of particles that have been "tagged" by imaging those particles at two discrete times across which they are displaced by some amount. Similarly to pressure sensitive paint, MTV takes advantage of the fluorescence and phosphorescence of excited molecules. However, rather than exciting molecules via ultraviolet light, these molecules are excited using a laser pulse. The wavelength of the laser pulse required depends on the target molecule. There are numerous types of MTV, including acetone seeded MTV, krypton tagging velocimetry (KTV), femtosecond laser electronic excitation tagging (FLEET), etc. Fundamentally, all of these techniques operate on the same principle: a laser is pulsed through a region of interest creating an illuminated line known as the "write" line. This line of energized particles propagates with the movement of the flow, and a subsequent image is captured of the line. The second image of the line is referred to as the "read" line. The displacement between the "write" and "read" lines along with the known frame rate of the camera allows for the calculation of a velocity profile using the simple distance over time relationship. For an in depth discussion of the theory and application of MTV, the author directs the reader to Chapter 14 of *Optical Diagnostics for Reacting and Non-Reacting Flow: Theory and Practice* [46].

At UTSI, significant work has been conducted using FLEET and acetone MTV in their high-speed facilities, particularly on characterizing the boundary layer that forms on the

Approved for Public Release; Distribution Unlimited. Case Number AFRL-2024-5997; Cleared 10/25/2024.

tunnel floor. Siddiqui and Gragston [57] were able to use a diffractive optical element to create a multi-point FLEET measurement at a 1 kHz sampling rate to measure the velocity profile near the floor of the UTSI Mach 4 Ludwieg Tube. They sampled at discrete locations starting at 7 mm above the tunnel floor and extending above the turbulent boundary layer into the freestream. They found that their measured velocity profile matched well with theoretical turbulent floor boundary layer predictions. Gragston and Smith [19] performed similar experiments using acetone MTV at a 10 kHz sampling rate, and they were able to obtain velocity measurements for both the freestream and boundary layer. Their results compared favorably to isentropic theory for the freestream velcocity. The boundary-layer thickness determined from the measured velocity profile compared favorably to schlieren imaging of the floor boundary layer. Notably, they were limited to probing 7 mm above the tunnel floor and higher due to low signal-to-noise ratio below the 7 mm height.

For the present experiment, the goal was to measure the boundary layer profile approximately 17.5 inches ($\sim 7\delta_{99}$) upstream of the ramps along the centerline of the tunnel using acetone MTV. Unfortunately, the pulse-burst laser required for this experiment had several component failures which rendered it inoperable. Given the long lead times and expense involved with ordering replacement parts for the laser, the MTV experiments were canceled.

2.2 Analytical Methodology

The following section details the data reduction techniques applied to the raw data collected from each of the diagnostic techniques described in Section 2.1.

2.2.1 Oil Flow Visualization

Due to the nature of oil flow visualization, there is little data reduction that can be done to gain further insight quantitatively. However, the following techniques were used to make approximations of characteristics relevant to three-dimensional SBLIs. Using a single image taken from the end of the steady-state portion of the tunnel run and a spatial resolution determined by a scale image, the approximate shock standoff distances at the ramp centerline

Approved for Public Release; Distribution Unlimited. Case Number AFRL-2024-5997; Cleared 10/25/2024.

were determined. Additionally, the same instantaneous images were contrast adjusted in ImageJ in order to visualize the separation and reattachment shocks. These images were then imported into MATLAB®, and lines were superimposed over the separation shock, reattachment shock, and upstream influence. The intersection of these lines identified the approximate location of the virtual conical origin (VCO).

2.2.2 Pressure Transducers

The reduction of the pressure transducer data began with the implementation of a calibration curve. As mentioned in Section 2.1.4, the calibration curves for the pressure transducers were produced by recording raw voltage data at known pressure conditions. The pressure and voltage data were imported into MATLAB® and had a linear curve fit applied to them. All of the raw voltage data were passed into this curve fit as an input and converted into a time history of pressure data.

2.2.3 Pressure Sensitive Paint

Reduction of the PSP data began with an image registration process. As the Ludwieg Tube is large scale and situated several feet off the ground, there is non-negligible motion that occurs during each run. To account for the tunnel motion, a fiducial marker is placed adjacent to the painted area on each model. This marker is tracked throughout each acquired image. A cross-correlation method is used to find the pixel offsets at each frame of the steady-state portion of the tunnel run. Each of these images are shifted such that they align with the calibration image acquired before the run.

Given the large scale of the model and inclination of the ramp face, a single calibration curve could not be applied uniformly to the PSP as this would yield inaccurate pressure values during the data reduction (e.g., negative values). This issue was resolved by performing the calibration on a pixel-by-pixel basis, where each pixel within the image has its own set of Stern-Volmer coefficients. However, this method is computationally expensive to perform. In order to alleviate these issues, a downsampling process is used to reduce the overall image size. In the present study, the PSP images are downsampled by factors of 3 in both

Approved for Public Release; Distribution Unlimited. Case Number AFRL-2024-5997; Cleared 10/25/2024.

directions: each pixel in the downsampled image is the unweighted average of a 3×3 region in the original. In this manner, the image size is reduced by a factor of 9, and the time required to create calibration curves for each pixel is greatly reduced.

The "wind-on" images are downsampled using the same process as the calibration images. For the conversion to pressure, each pixel intensity from the "wind-on" images are divided into their respective reference pixel intensity from the calibration image. This ratio (I_{REF}/I) is then input into the modified Stern-Volmer relationship, shown in Eq. 2.1, and the resulting pressure ratio is multiplied by the known reference pressure (P_{REF}) to produce the measured pressure value (P). This process is repeated for each pixel location within a single image and for each acquired "wind-on" image. Once each image in the set is converted to pressure, the average and standard deviation of the image sets are computed.

2.3 Uncertainty Analysis

2.3.1 Pressure Transducers

Estimates of the measurement uncertainties for the two pressure transducers (i.e., Kulites) used in this experiment were based upon the manufacturer-reported errors. Both sensors (model numbers XCE-080 and XCE-062) reportedly have combined non-linearity, hysteresis, and repeatability errors of ±0.1% of their nominal 100 mV full-scale output (FSO) values. The XCE-080 was rated for operating pressures ranging from 0–0.35 bara (0–5 psia). The error resulting from the manufacturer specifications is then ±0.00035 bara (±0.005 psia). The XCE-062 was rated for operating pressures ranging from 0–10 psia with a resulting error of ±0.01 psia.

The Druck DPI612 pressure calibration unit was used as the "truth" measurement for calibrating both the Kulites and the PSP. This instrument has a manufacturer-reported uncertainty of 0.052% of the 30 psia nominal FSO value. The data acquisition system was set to record voltages over a range of ±10 V, and as PXIe-6358 has a 16-bit analog-to-digital (A/D) converter, it has a resolution uncertainty of ±0.305 mV. The measurement uncertainties of the data acquisition system are negligible as the propagation of these

Approved for Public Release; Distribution Unlimited. Case Number AFRL-2024-5997; Cleared 10/25/2024.

uncertainties results in virtually no change in the overall uncertainty of the pressure measurements. The uncertainty of these measurements are primarily dominated by the uncertainties reported for the Kulite transducers and Druck calibration unit. When the uncertainties of the Kulites and Druck are combined via the root-sum-square (RSS) formulation, the reported total uncertainties in the pressure transducers for this experiment become ±0.016 psia for the XCE-080 and ±0.019 psia for the XCE-062. These are the uncertainty bounds for an individual measurement point acquired by the transducers. In calculating an average over N measurement points, the reported uncertainties would then be reduced by a factor of $1/\sqrt{N}$ [29, 65].

2.3.2 Pressure Sensitive Paint

The PSP diagnostic technique utilized in these experiments can be subject to human-error during the paint application process due to the inherent inconsistencies associated with the use of a manually-operated sprayer including differences of paint spray angle, distance from the target, and the total number of spray passes over the surface for each application. The culmination of these inconsistencies can translate into variations in paint thickness, roughness, and overall uniformity which may impact the response characteristics of the paint. This error is rather difficult, if not impossible, to accurately quantify. In an effort to maintain consistency between experiments, a strict set of procedures were implemented to ensure that the paint application was as uniform as possible.

An ideal PSP experimental setup would have the ultraviolet (UV) excitation and the camera recording response positioned such that they are both normal to the entire painted region of interest. For the present set of experiments, this is not possible given the incline of the ramp surface as well as available optical access for the LEDs to illuminate the model see Fig. 2.7). In short, the camera captures a two-dimensional representation of a three-dimensional object, and there is likely some amount of uncertainty introduced by the three-dimensionality of the model. To alleviate these effects, the pixel-by-pixel calibration process was implemented as discussed in the previous section.

The uncertainties associated with the PSP image acquisition, calibration, and conversion to pressure are all encapsulated within the *in situ* calibration process. Static calibration

Approved for Public Release; Distribution Unlimited. Case Number AFRL-2024-5997; Cleared 10/25/2024.

images that were acquired at ∼2.5 psia (i.e., the pressure expected on the ramp surface) and ∼0.5 psia (i.e., the pressure expected on the floor ahead of the interaction) were used to quantify the uncertainties of the PSP applications used in this experiment. Intensity values from locations both on the tunnel floor and on the ramp surface were collected and converted to pressure using their corresponding pixel-specific calibration curve. The raw intensity values were used in determining the random errors associated with image acquisition, and the converted pressure values were used in determining the bias errors introduced by the curve fit which contains several contributing variables including I,I_{REF}, and P_{REF}. The random errors (U_P) and the bias errors (B) were combined through the root-sum-square (RSS) formulation (Eq. 2.2) to determine the total uncertainty in the pressure measurement.

$$U_{total} = \sqrt{U_P^2 + B^2} \tag{2.2}$$

The random uncertainties of the intensities acquired by the camera are calculated using the following methodology. First, various pixels across the imaging region (both on the floor and on the ramp surface) were probed to collect intensity values across the calibration image set. The uncertainties of these intensities are calculated using Eq. 2.3, where σ is the standard deviation of the intensity values, t is the students' t-distribution value at 95% confidence level, and N is the number of samples. The number of samples corresponds to the number of images used in the calibration process; for these experiments, $N = 81$ images. An identical process is used to evaluate the uncertainties in the reference image at the same pixel locations.

$$U_I = \frac{t \cdot \sigma_I}{\sqrt{N}} \tag{2.3}$$

The intensities collected from the calibration images are input into their corresponding calibration curves to convert the values to pressure. The bias error introduced by PSP calibration is the difference between the converted pressure (averaged over N samples) and the known pressure condition from the Druck. This relationship is shown in Eq. 2.4.

$$B = |P_{Druck} - P_{avg}| \tag{2.4}$$

The conversion to pressure via the Stern-Volmer relationship shown in Equation 2.1 involved both the image intensity and reference image intensity. Since these values have known uncertainties (found via Eq. 2.3), the propagation of these errors into the pressure conversion must be accounted for in determining the total uncertainty. The general form of the error propagation is shown in Eq. 2.5, where U is the uncertainty and R represents the desired variable that has a known functional dependence on x_i which represents the known/measured variables.

$$U_R = \sqrt{\sum_{i=1}^{n} \left(U_{x_i} \frac{\partial R}{\partial x_i} \right)^2} \tag{2.5}$$

Applying the error propagation method to the Stern-Volmer equation (Eq. 2.1) yields the form shown in Eq. 2.6.

$$\begin{aligned} U_{\frac{P}{}}^2 = & \left[U_{\overline{I}} \left(\frac{-2P_{REF}A_2\overline{I_{REF}}}{\overline{I}^3} - \frac{P_{REF}A_1\overline{I_{REF}}}{\overline{I}^2} \right) \right]^2 \\ & + \left[U_{\overline{I_{REF}}} \left(\frac{2P_{REF}A_2\overline{I_{REF}}}{\overline{I}^2} + \frac{P_{REF}A_1}{\overline{I}} \right) \right]^2 \end{aligned} \tag{2.6}$$

For the values extracted from the PSP on the ramp surface, typical random error values (expressed as a percentage of the known Druck pressure) were found to be 0.65%. Typical bias errors for the same pixel were 3.50%. The combined uncertainties, calculated using Eq. 2.2, were then 3.57%. For the PSP measurements on the floor, typical random error values were 2.03%, and bias errors were 19.01% (expressed in terms of the known Druck pressure). The combined total uncertainties were then 19.12%. The ramp pressure uncertainties were based on a pressure values of 2.5 psia while the floor pressure uncertainties were based on a pressure value of 0.5 psia. For the expected pressure values on the floor during the steady-state, there is a fairly substantial bias error as a result of the calibration process. However, when comparing the bias errors in absolute units, the uncertainty is approximately the same value as that on the ramp, ± 0.0875 psia. As will be discussed in the latter portion of Chapter 3, the PSP measurements have high correlation and coherence compared to the Kulite pressure values when both are mean-subtracted. Generally, the PSP

Approved for Public Release; Distribution Unlimited. Case Number AFRL-2024-5997; Cleared 10/25/2024.

is able to appropriately respond to fluctuating pressure content, although caution should be taken when reporting absolute pressure values measured by PSP.

Approved for Public Release; Distribution Unlimited. Case Number AFRL-2024-5997; Cleared 10/25/2024.

Chapter 3

Results and Analysis

The following section contains the results collected and analyzed via the processes outlined in Chapter 2. Note that the results shown here pertain to the low sweep ramp ($\lambda = 10°$) and the high sweep ramp ($\lambda = 27.5°$). The results from the unswept ramp ($\lambda = 0°$) have been omitted. This omission is a result of two difficulties encountered during the collection of these data. First, the unswept ramp data from the initial experiment were lost due to a hard drive malfunction. Second, during the recollection of these data, the unswept ramp was damaged by a large section of diaphragm and less than 50% of the steady-state duration for a single run were able to be processed. As a result, the author has chosen to omit the limited results obtained for the unswept ramp in favor of referencing existing literature.

3.1 Oil Flow Visualization

Figure 3.1 shows typical instantaneous images from the oil flow visualization experiments for both swept compression ramps in UTSI's Mach 4 Ludwieg Tube. These plots are configured with the flow direction being left to right and with axes aligned such that the origin is on the tunnel centerline at the ramp face. The x- and z-coordinates are non-dimensionalized by $\delta_{99} = 2.5$". The limit of the z-axis was extended to visualize the VCO location. The edge of the camera field of view (FOV) is shown for both cases. As the steady-state flow duration is approximately 120 ms, the streaklines from the present experiment will not be as well-defined as one would expect to see from a longer duration wind tunnel experiment. However, the streaklines that are visible reveal clear differences in the separation region shapes between the low sweep ramp ($\lambda = 10°$) and the high sweep ramp ($\lambda = 27.5°$). The low sweep case

Approved for Public Release; Distribution Unlimited. Case Number AFRL-2024-5997; Cleared 10/25/2024.

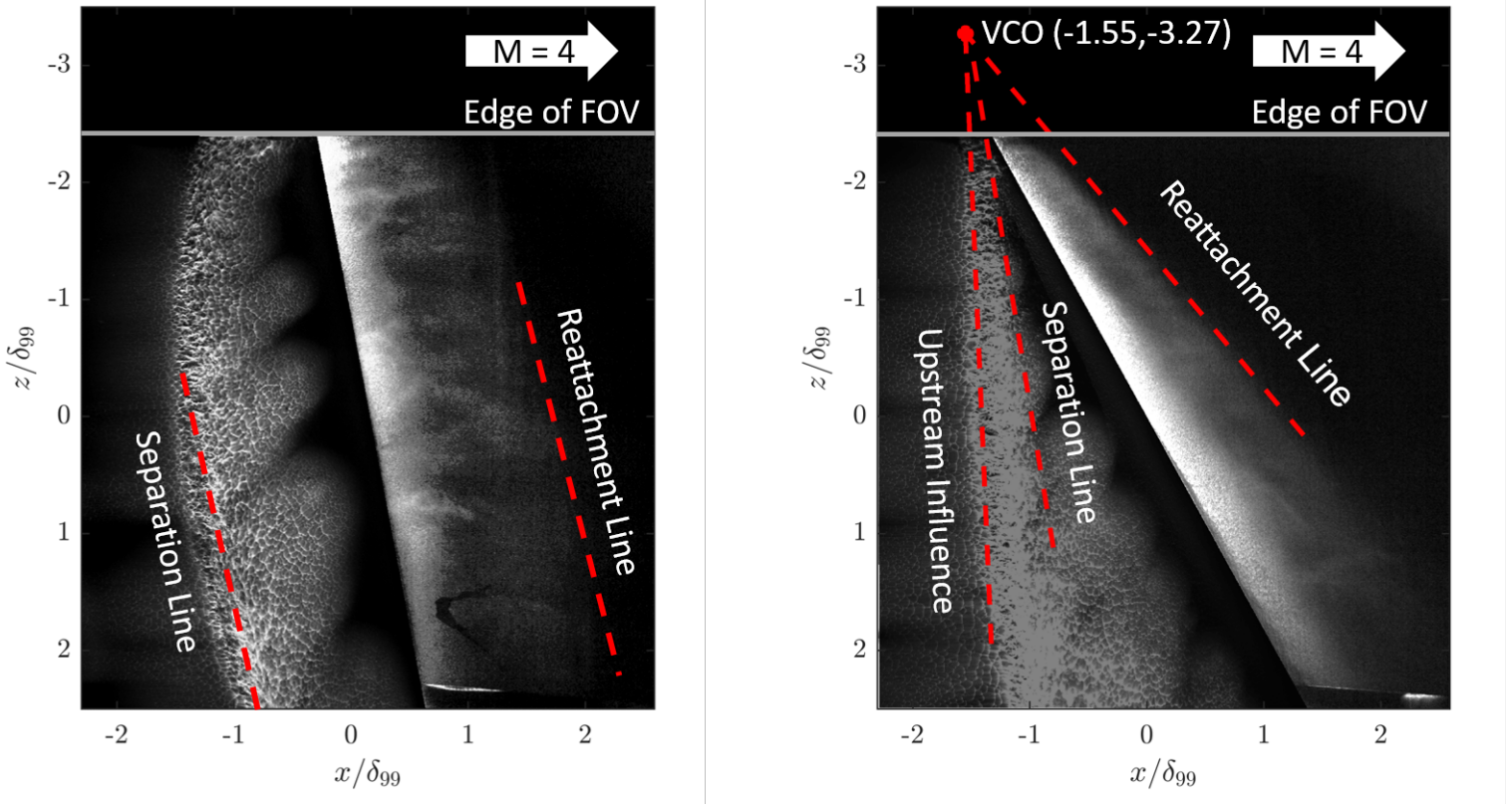
shown in Figure 3.1a exhibits cylindrical symmetry typical of a closed interaction (i.e., the separation and reattachment lines are approximately parallel to each other), whereas the high sweep case shown in Figure 3.1b shows a clear pattern of quasi-conical symmetry typical of an open interaction (i.e, the separation and reattachment lines diverge from each other in the spanwise direction).

The reattachment line locations were determined by contrast adjusting the images such that the reattachment lines were more easily discernible. The approximate separation shock location was determined from these images that have a resolution of 0.012 inches/pixel. The separation line location along the centerline for the low sweep case was about 3.6" ($\sim 1.4\delta_{99}$) upstream of the ramp, whereas it was about 3.1" ($\sim 1.2\delta_{99}$) upstream of the ramp in the high sweep case. Interestingly, Allen *et al.* [2] showed that the separation shock location moves further upstream as sweep angle increases for compression ramps at Mach 2. However, as Allen *et al.* [2] noted, the quasi-conical symmetry of highly swept ramps means that the separation region increases in size as the flow moves in the spanwise direction. Ultimately, this means that the separation region length on the centerline is also dependent on the distance from the virtual conical origin as well as the inviscid shock strength.

3.2 Pressure Sensitive Paint

Results from the PSP experiments are shown in Figs. 3.2 and 3.3 which contain the average surface pressure distributions and fluctuating surface pressure contours (P'_{RMS}), respectively. The P'_{RMS} values are identically equivalent to the standard deviation of the pressures. All pressures reported in this section are in units of absolute pressure. The plots are configured with the flow direction being left to right and with axes aligned such that the origin is on the tunnel centerline at the ramp face. The x- and z-coordinates are non-dimensionalized by $\delta_{99} = 2.5$". All PSP data used in these analyses were collected during the steady-state portion of the tunnel run (i.e., over approximately 120 ms). Figures 3.2a and 3.3a show the average and P'_{RMS} pressures for the $\lambda = 10°$ sweep case. Figures 3.2b and 3.3b show the average and P'_{RMS} pressures for the $\lambda = 27.5°$ sweep case.

Approved for Public Release; Distribution Unlimited. Case Number AFRL-2024-5997; Cleared 10/25/2024.

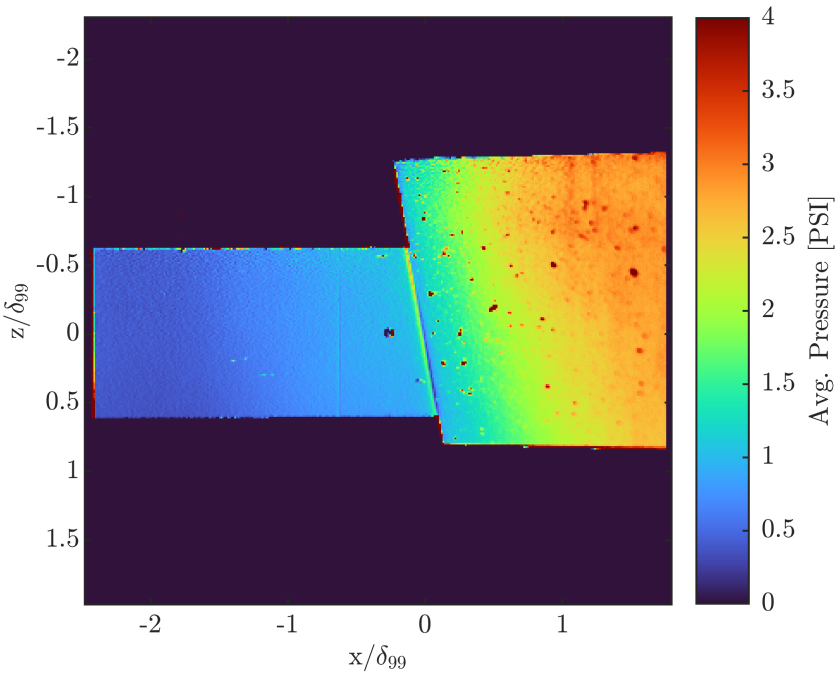


(a) 10° Sweep

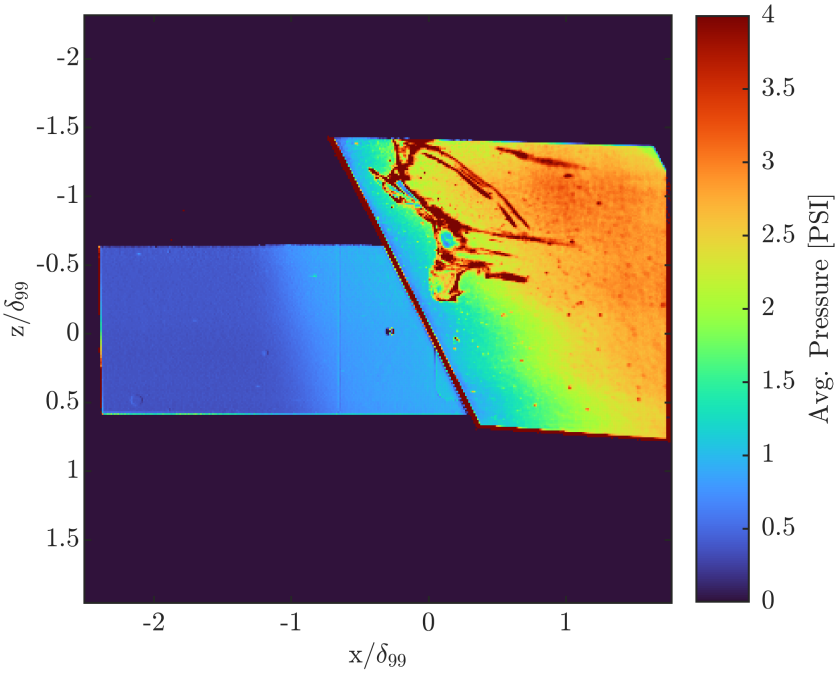
(b) 27.5° Sweep

Figure 3.1: Oil flow visualizations on the two swept compression ramps. The approximate location of the Virtual Conical Origin (VCO) is identified on the highly swept case.

Approved for Public Release; Distribution Unlimited. Case Number AFRL-2024-5997; Cleared 10/25/2024.



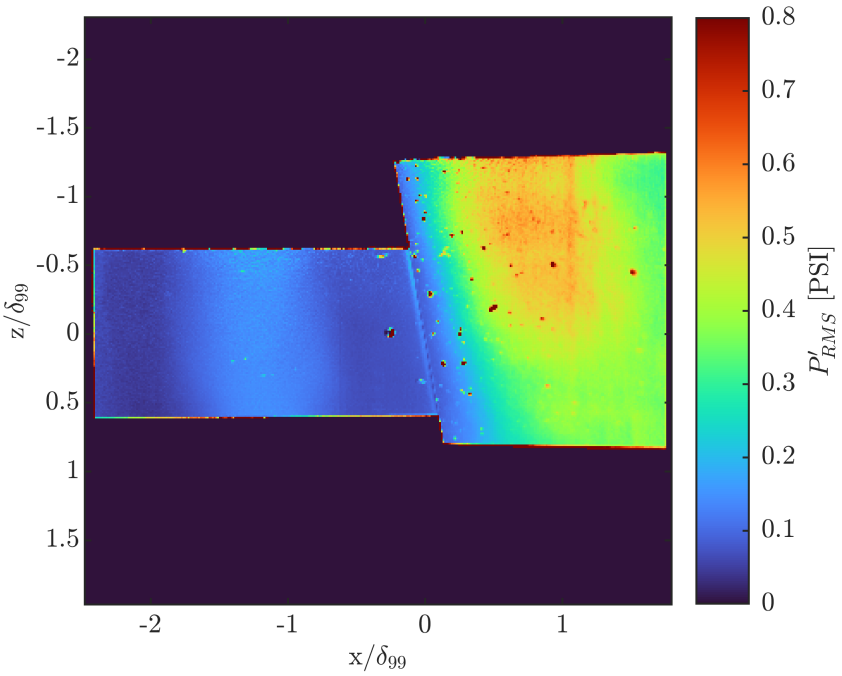
(a) $\lambda = 10°$



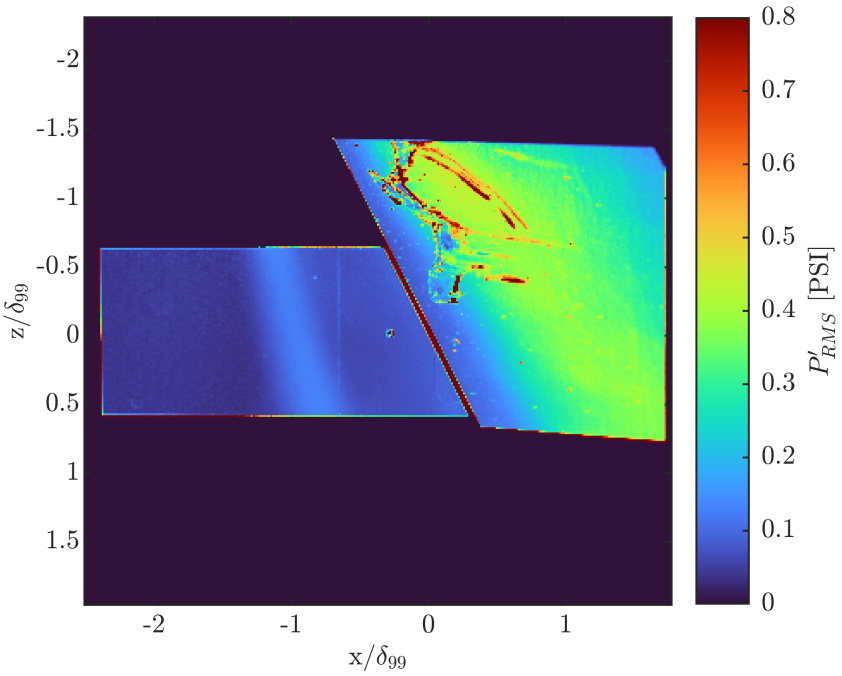
(b) $\lambda = 27.5°$

Figure 3.2: Average surface pressure distribution obtained over 2400 frames from the steady-state conditions run for both swept ramps.

Approved for Public Release; Distribution Unlimited. Case Number AFRL-2024-5997; Cleared 10/25/2024.



(a) $\lambda = 10°$



(b) $\lambda = 27.5°$

Figure 3.3: P'_{RMS} (pressure fluctuation) contours obtained over 2400 frames from the steady-state conditions run for both swept ramps.

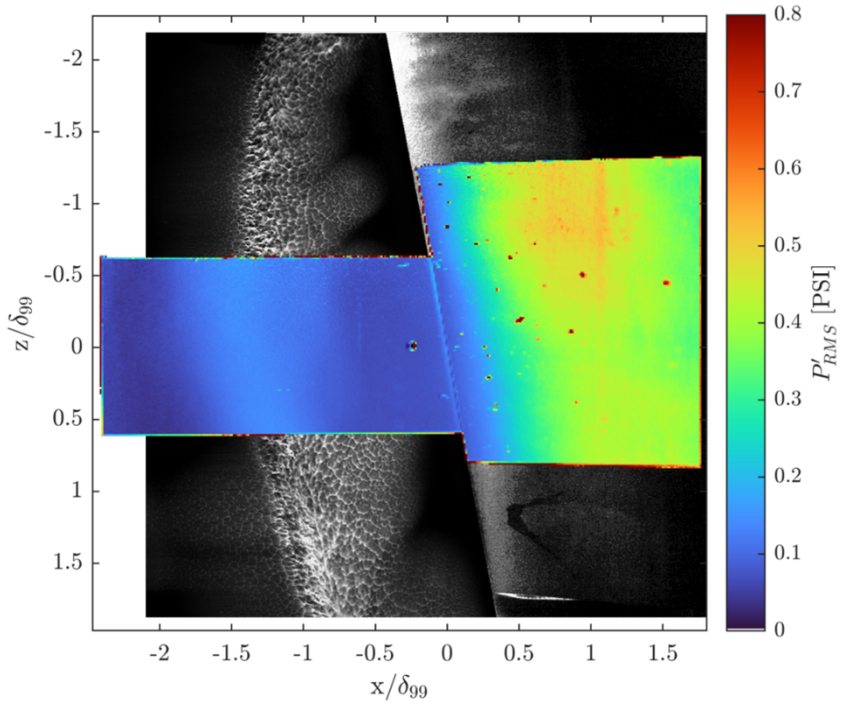
Approved for Public Release; Distribution Unlimited. Case Number AFRL-2024-5997; Cleared 10/25/2024.

Note that some damage to the painted surface in Figure 3.2b was the result of a diaphragm segment striking the model surface during the previous run. The surfaces outside of the obvious damage are still pristine and should not be affected, and the paint did respond as expected throughout the data reduction process.

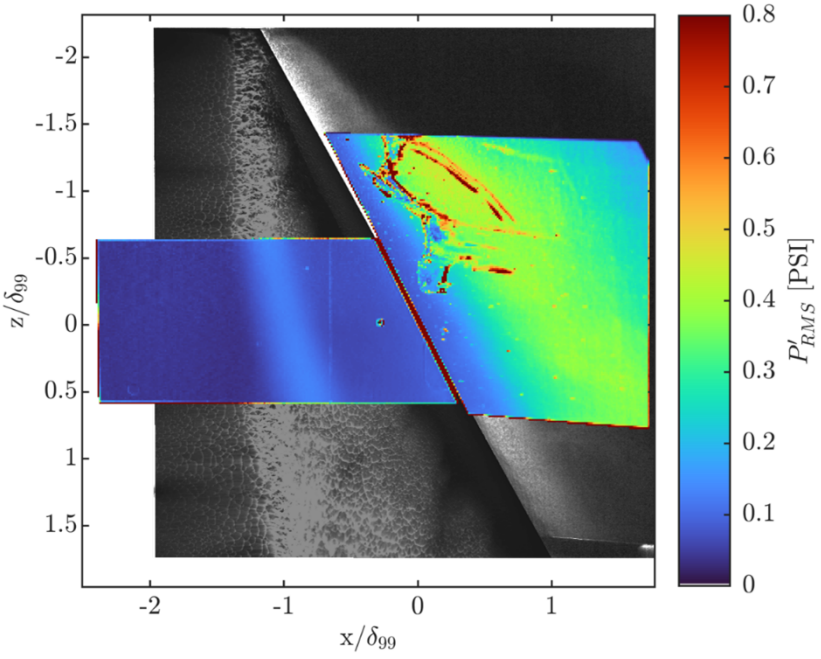
Qualitatively, the average pressure fields in Figure 3.2 show the expected behavior of a relatively low pressure upstream of the separation region, higher pressure within the separation region, and an additional pressure rise within the reattachment region. Considering the fluctuating pressure fields shown in Figure 3.3, one can see brighter bands upstream of the ramp that mark the beginning of the separation region as indicated by the elevated unsteadiness within this region. The band is noticeably wider in the low sweep case (Figure 3.3a), as this corresponds to a larger region of unsteadiness; this agrees with the results obtained by Erengil and Dolling [12]. The regions of unsteadiness that are evident in the P'_{RMS} contours match with the locations of the separation and reattachment shocks determined by the oil flow experiments as shown in the direct comparisons made within Figure 3.4. In both cases, the increased pressure fluctuations upstream of the ramp face correspond well to the approximate separation line location determined by the oil flow.

In order to verify that the PSP response characteristics were sufficient to capture the unsteadiness in and around the separation region, a virtual pressure tap was created using the PSP data at a location directly upstream of the Kulite closest to the ramp face ($x/\delta_{99} \approx -0.3$). The virtual tap and Kulite pressures are compared to one another in Figures 3.5 and 3.6. Here, the steady-state time histories, cross-correlation coefficient functions, and mean-squared coherence of these data are shown for both ramps ($\lambda = 10°$ and $\lambda = 27.5°$). It is important to emphasize that the PSP data have been downsampled by averaging 3×3 regions across the images to reduce some of the random errors arising from noise within these data. The Kulite data are also lowpass filtered prior to their analog-to-digital conversion. The low sweep case has a maximum cross-correlation coefficient of 0.60 with an offset of one data point (Δt = 0.05 ms) as can be seen in Figure 3.5b, while the high sweep case has a maximum cross-correlation coefficient of 0.68 also with an offset of one data point (Δt = 0.05 ms) as seen in Figure 3.6b. In both cases, the virtual tap and Kulite pressures show reasonable coherence over a fairly broad band of frequencies.

Approved for Public Release; Distribution Unlimited. Case Number AFRL-2024-5997; Cleared 10/25/2024.

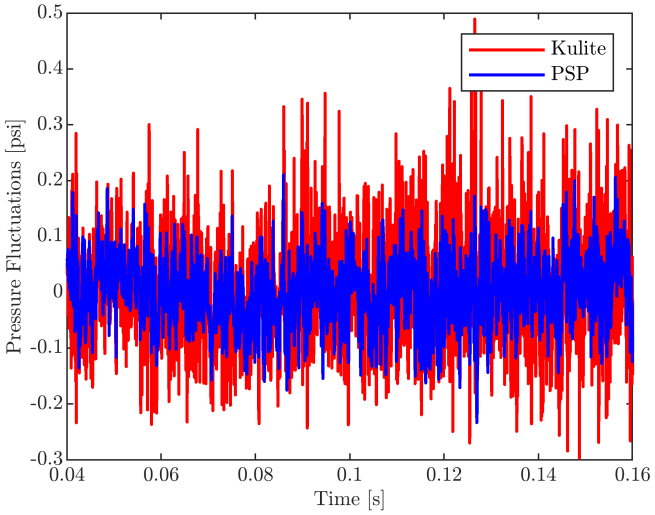


(a) $\lambda = 10°$

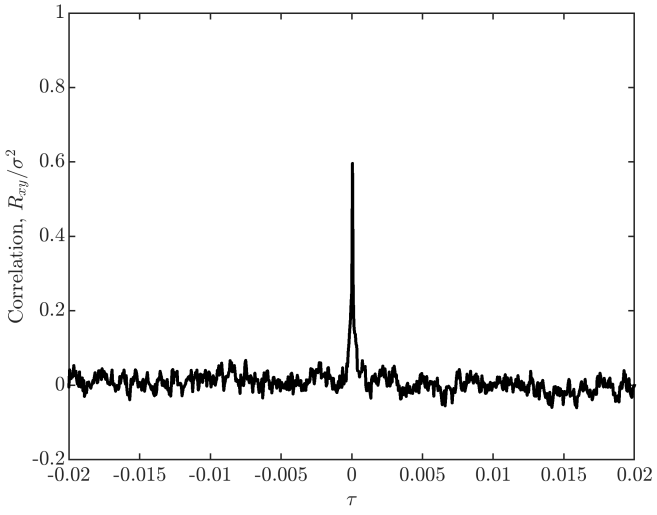


(b) $\lambda = 27.5°$

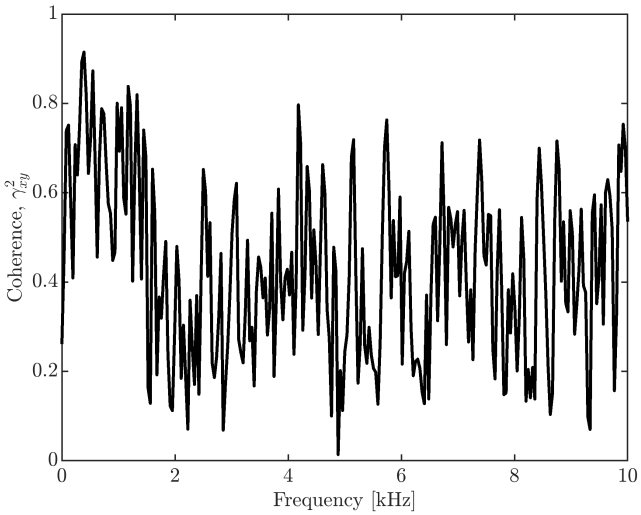
Figure 3.4: P'_{RMS} contours superimposed onto oil flow visualization images for both swept ramps.



(a) Time history



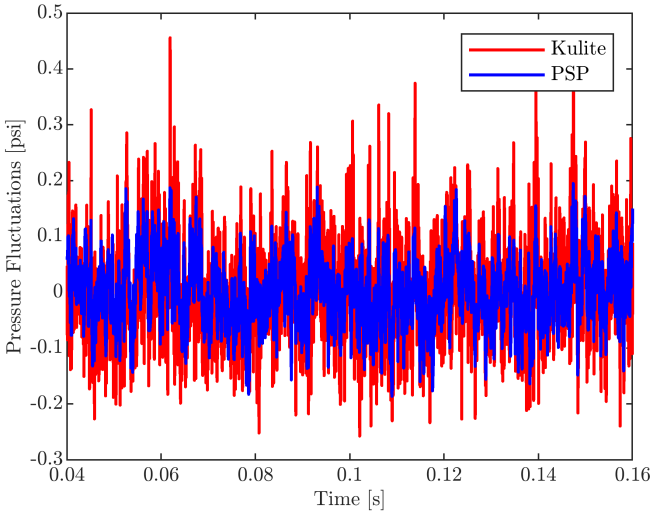
(b) Cross correlation



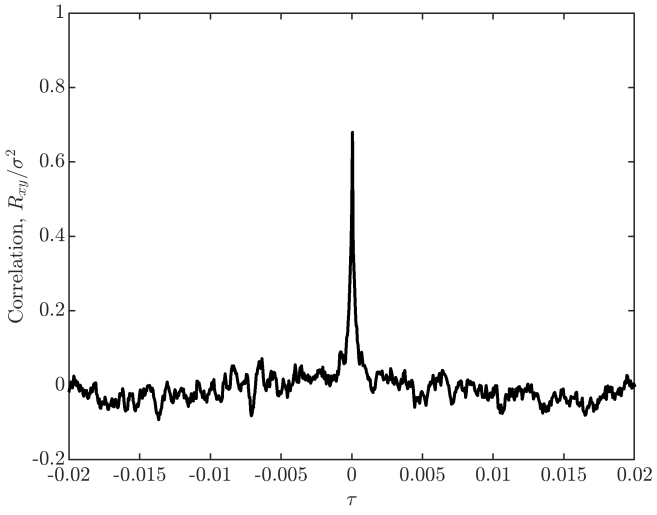
(c) Coherence

Figure 3.5: Example time history, cross correlation, and coherence of the PSP virtual tap and the Kulite within the separation region for the $\lambda = 10°$ sweep case.

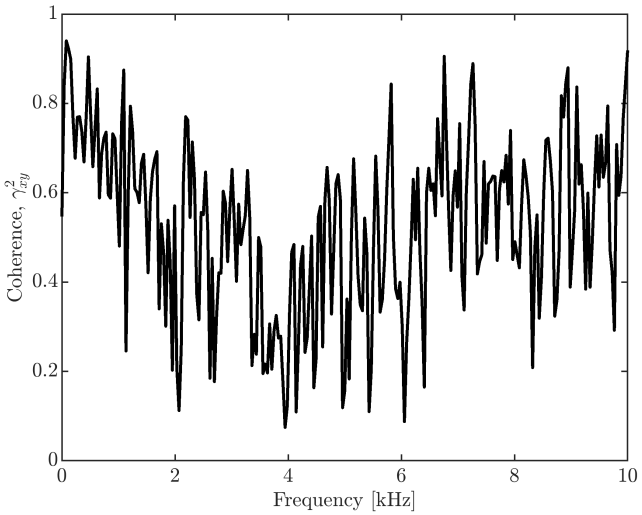
Approved for Public Release; Distribution Unlimited. Case Number AFRL-2024-5997; Cleared 10/25/2024.



(a) Time history



(b) Cross correlation



(c) Coherence

Figure 3.6: Example time history, cross correlation, and coherence of the PSP virtual tap and the Kulite within the separation region for the $\lambda = 27.5°$ sweep case.

Approved for Public Release; Distribution Unlimited. Case Number AFRL-2024-5997; Cleared 10/25/2024.

Overall comparisons of the time histories, cross-correlations, and coherence show that both the Kulite and PSP pressures can be used to characterize these shock interactions. However, as the PSP provides data over a much larger area, this diagnostic can be more useful in terms of characterizing the overall structure within such 3D interactions.

Using the unsteady pressure fluctuations shown in the P'_{RMS} contours in Figure 3.3, values were extracted from a line immediately adjacent to the Kulite. This data extraction line follows the freestream direction based on the incoming flow, remaining straight across the entire domain (i.e., it does not turn on the ramp to follow the local freestream direction). The values extracted from these data are shown in Figure 3.7. The large spikes in these plots result from discontinuities that occur at the interface between the ramp and the floor plate as well as the damage resulting from strikes of diaphragm material. In both the low sweep (Figure 3.7a) and high sweep (Figure 3.7b) cases, there are two local maxima that exist in broad peaks, and these correspond to the average separation and reattachment locations. The pressure fluctuations in the reattachment region are approximately three times larger than those in the separation region for both cases. Overall, the magnitude of the pressure fluctuations is greater in the low sweep case, however, and these fluctuations persist over a larger region in the streamwise direction than the high sweep case. Again, this corresponds well with the results found by Erengil and Dolling [12] and Allen *et al.* [2].

For direct quantitative comparisons between the present and historical data on similar highly-swept interactions, the P'_{RMS} values are plotted in a different manner in Figure 3.8. Here, the unsteady pressures are non-dimensionalized by the mean pressure from upstream of the interaction (i.e., $\bar{P}_{wo}$ according to Erengil and Dolling [12]). The resulting values are then plotted in a conical coordinate system with its origin set to the VCO location, which has been redefined with the PSP data (i.e., not using the VCO location from the prior oil flow visualizations). Erengil and Dolling [12], who tested ramp configurations with $\lambda \geq 25^\circ$ at Mach 5, found that by sampling a region normal to and across the separation shock with pressure transducers, the normalized standard deviation collapses regardless of where the samples are collected in the spanwise direction. An identical approach was used with the PSP data collected in this experiment, and the results are shown in Figure 3.8.

Approved for Public Release; Distribution Unlimited. Case Number AFRL-2024-5997; Cleared 10/25/2024.

Figure 3.8a shows the present PSP data and the sample regions that were selected normal to the separation shock and varying in the spanwise direction. The P'_{RMS} values were extracted from these lines and plotted in conical coordinates, as shown in Figure 3.8b, where θ is the angle of the line connecting the VCO to the point along the sample region that is being interrogated (i.e., the angle with respect to the positive z-axis). The tangent of this angle is the ratio between the x-coordinate and the z-coordinate of the interrogation point as referenced from the VCO. The sampled regions collapsed to the same line as expected, and the data from the present study have a similar shape when compared to the results of Erengil and Dolling [12]. Note that the current PSP results shown in Figure 3.8b do not fall directly in between the red and green lines which correspond to the data from Erengil and Dolling [12]. This can likely be attributed to the differences in Mach number and sweep angle between the two experiments, although there may be other contributing factors. Due to the experimental differences, it is not possible to isolate any particular parameter(s) that influence the unsteadiness in highly swept ramp interactions. It may be possible that the normalized pressure fluctuations are dependent on an 'effective' shock strength determined by incoming Mach number, compression angle, and sweep angle. Further investigation and experimentation would be required to confirm this and to determine what, if any, empirical relationship exists to relate these parameters.

Having pressure data from PSP across the entire interaction region allows one to extract additional quantitative data such as the location of the separation shock foot. The instantaneous shock foot location is determined by finding the first point in the streamwise flow direction (left to right) at which the pressure exceeds 150% of the freestream value (i.e., where $P/P_\infty \geq 1.5$). This value was chosen based on similar shock foot tracking methods performed by Vanstone *et al.* [60] and Erengil and Dolling [12]. The probability density functions (PDFs) for both the low and high sweep cases are presented in Figs. 3.9a and 3.9b, respectively. The PDFs for each of the cases have been mean-subtracted and subsequently normalized by the standard deviation of the shock location. Each PDF uses 2400 data points of the shock position extracted from the PSP images, and 30 bins are used to plot these histograms. The solid black line shows the behavior of a Gaussian distribution for comparison. In both cases, the separation shock motion appears to be normally distributed

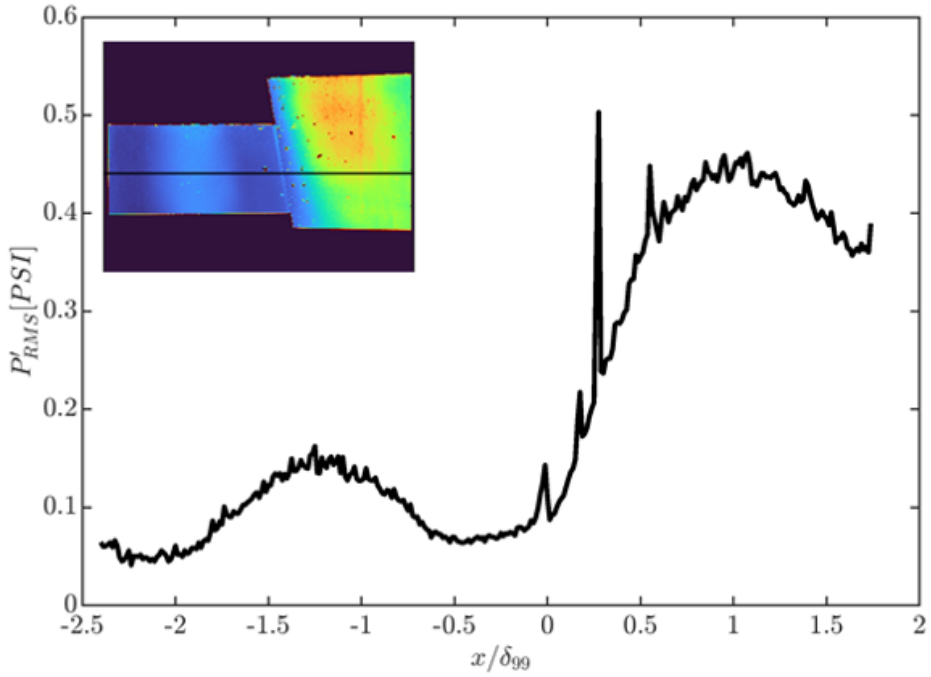
Approved for Public Release; Distribution Unlimited. Case Number AFRL-2024-5997; Cleared 10/25/2024.

with slight variations that are easily attributed to experimental uncertainties and binning errors. These results compare favorably to those of Erengil and Dolling [12] who found similar behaviors for swept ramp configurations at Mach 5 conditions.

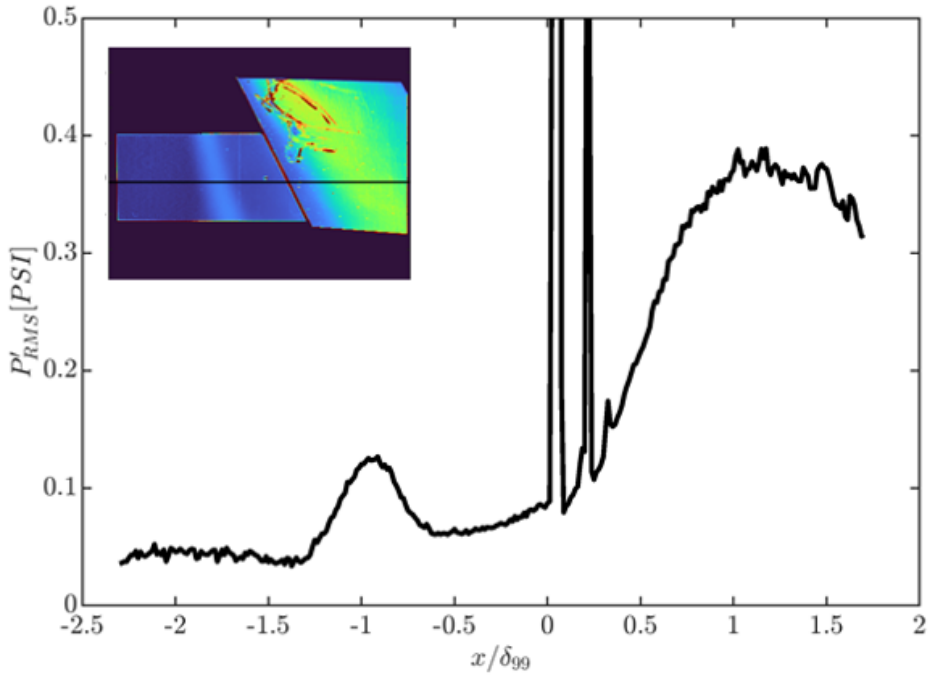
Power spectral densities of the separation shock motion for both the low and high sweep cases are shown in Figs. 3.10a and 3.10b, respectively. These spectra have been pre-multiplied by the frequency (vector) and normalized by the variance of the data. The PSDs are calculated using Welch's method with 512 points used in each fast Fourier transform calculation, and those data are windowed with Hann windows using 75% overlap. In total, this means that 2304 points were used in creating the PSDs (recall that 2400 data points were collected from steady-state). With the data sampled at 20 kHz, the resulting frequency resolution is approximately 39 Hz. The zero-crossing frequencies are computed from the mean-subtracted separation shock location, and these values are denoted by the vertical, dashed lines in Figure 3.10. The zero-crossing frequencies are non-dimensionalized using two methodologies to yield different forms of the Strouhal number. The first, St_δ, uses the incoming boundary layer thickness as the characteristic length scale. The second, St_L, uses the intermittent length, which is defined as the distance over which the separation shock foot traverses in the streamwise direction, as the characteristic length scale.

The low sweep case yielded zero-crossing frequencies ranging from 200–400 Hz, which correspond to $St_\delta \approx 0.02$–0.04 and $St_L \approx 0.03$–0.06. The high sweep case exhibited zero-crossing frequencies ranging from 700–800 Hz, which correspond to $St_\delta \approx 0.07$ and $St_L \approx 0.03$. Vanstone *et al.* [60] found their 22.5° swept ramp to have a $St_\delta \approx 0.03$ in a Mach 2 freestream. Their results compare well to the current low sweep case, but there are significant differences for the high sweep case. However, the St_L values for both the low and high sweep cases fall within bounds of $0.02 \leq St_L \leq 0.05$, which are typical to turbulent SBLIs according to Clemens and Narayanaswamy [7] and Dussauge *et al.* [10]. This seems reasonable as the intermittent length scale (which is used to non-dimensionalize these frequencies) can vary significantly with sweep angle, allowing this Strouhal number to scale with the dynamics of the interaction. On the contrary, this scaling would not be captured by the St_δ parameter because the sweep angle has no bearing on the incoming boundary layer thickness.

Approved for Public Release; Distribution Unlimited. Case Number AFRL-2024-5997; Cleared 10/25/2024.



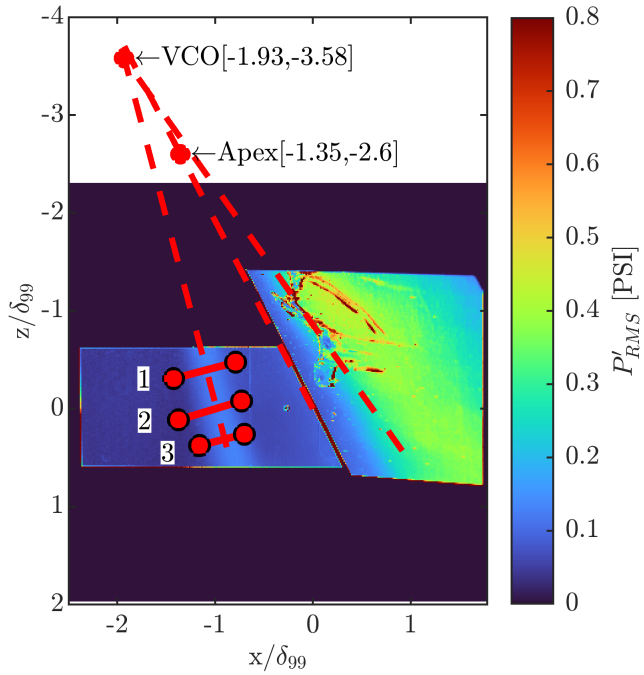
(a) $\lambda = 10°$



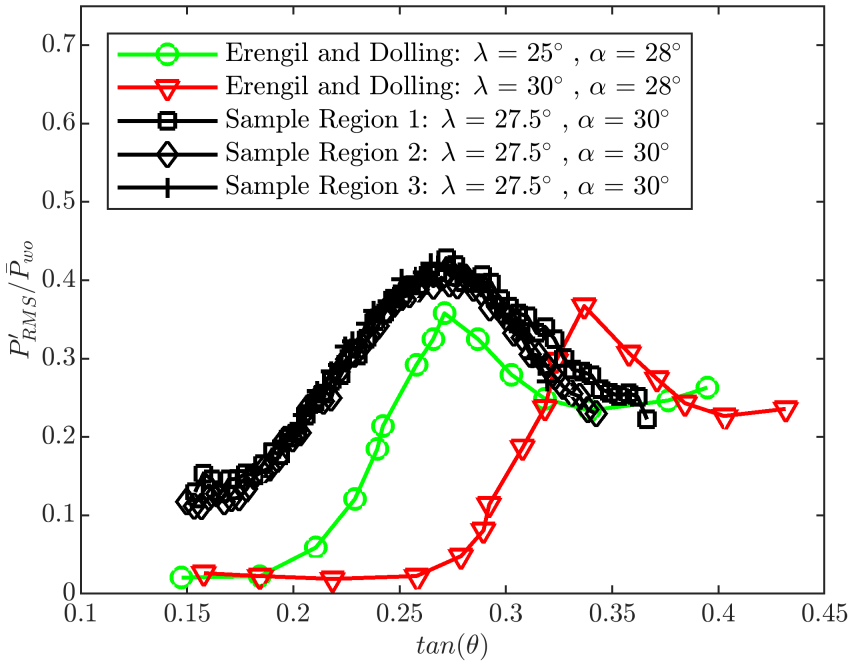
(b) $\lambda = 27.5°$

Figure 3.7: Traces of P'_{RMS} extracted along $z/\delta_{99} = 0.05$ for both ramps. The large spikes are a result of discontinuities in the paint at the ramp-floor interface and damage to the surface by diaphragm particles.

Approved for Public Release; Distribution Unlimited. Case Number AFRL-2024-5997; Cleared 10/25/2024.



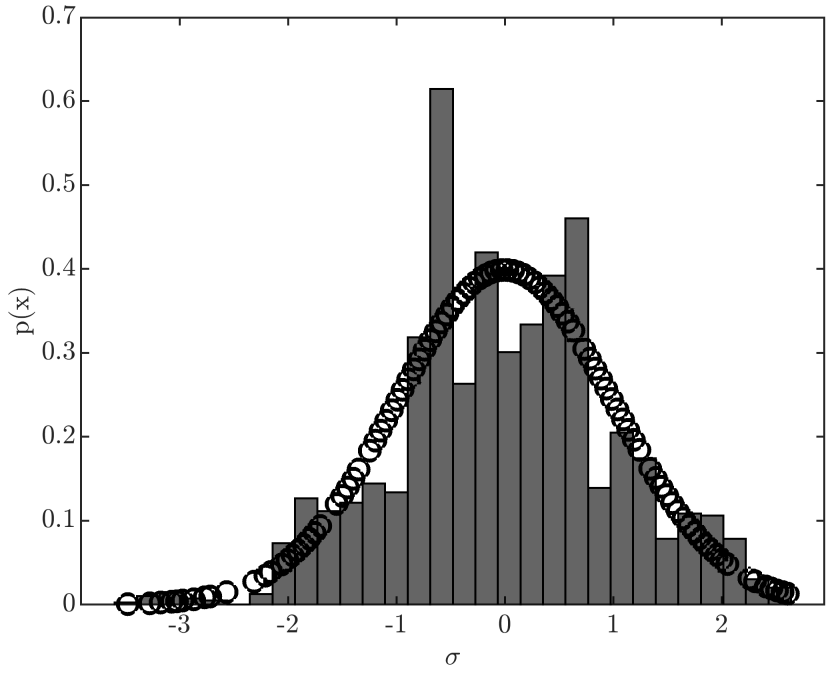
(a) Footprint of the shock interaction region and sample locations superimposed on the P'_{RMS} image for $\lambda = 27.5°$



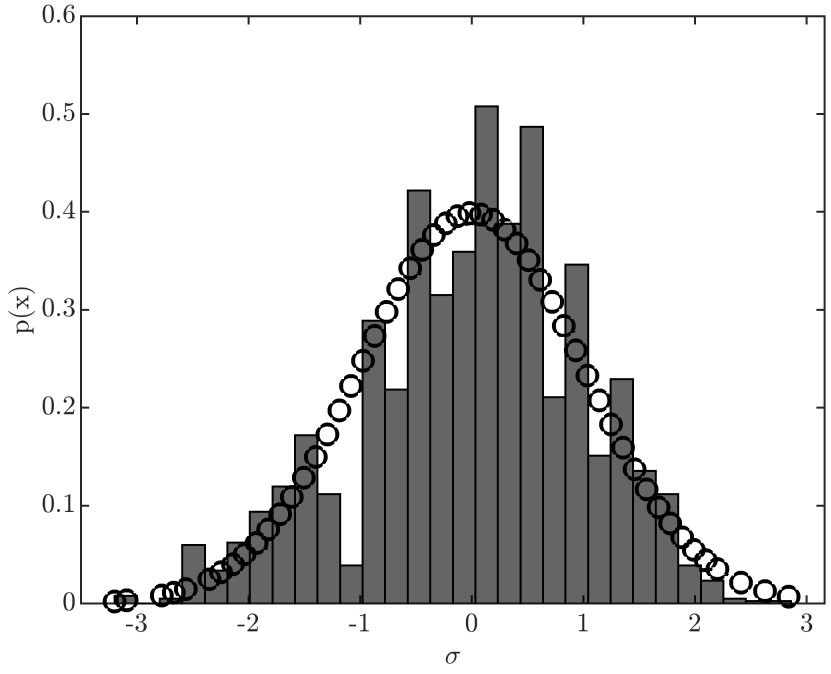
(b) Normalized pressure fluctuations from the three sample locations compared to prior results of Erengil and Dolling [12]

Figure 3.8: Comparison of highly-swept ramp interactions from the current experiment and results from Erengil and Dolling [12].

Approved for Public Release; Distribution Unlimited. Case Number AFRL-2024-5997; Cleared 10/25/2024.



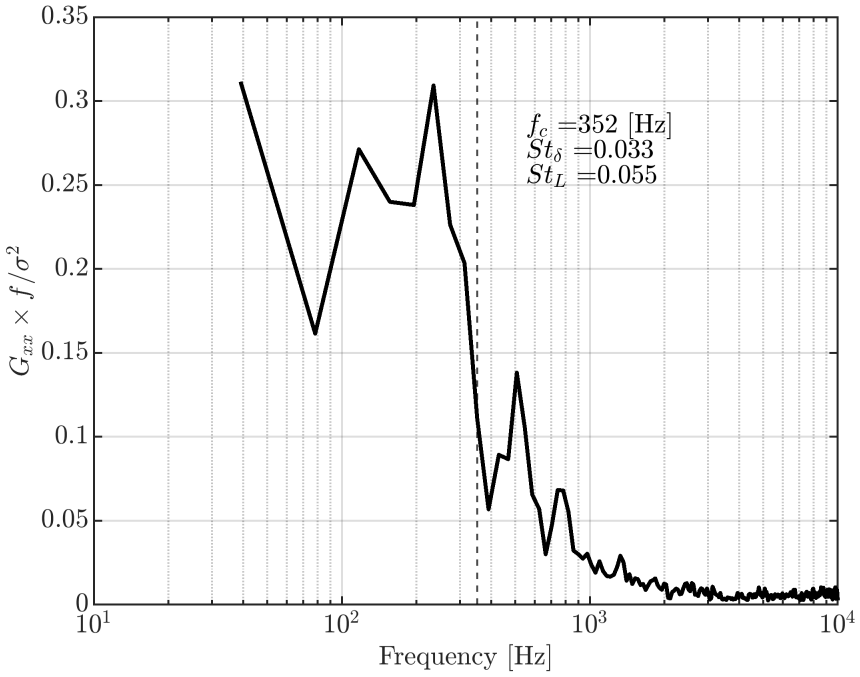
(a) PDF for $\lambda = 10°$



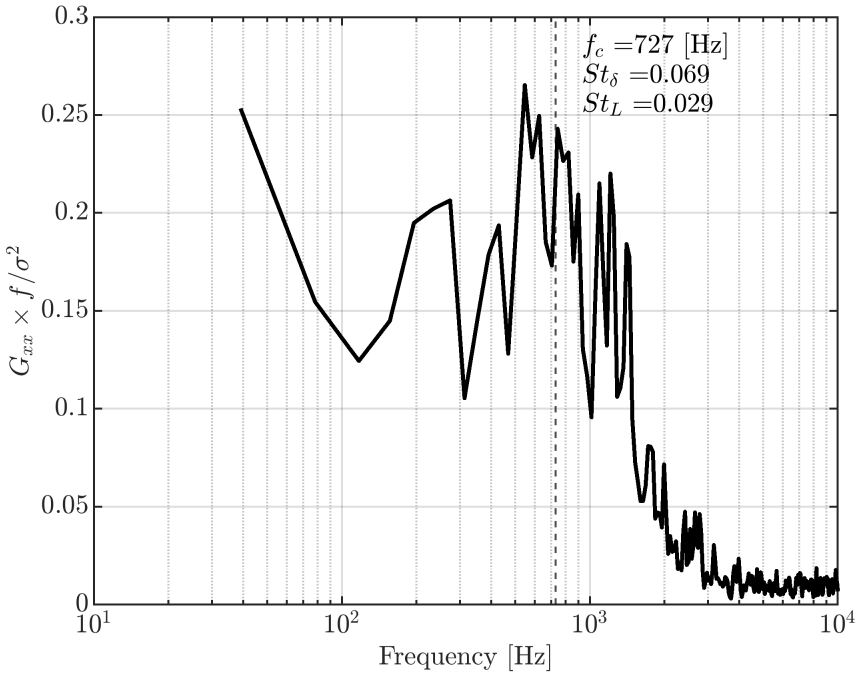
(b) PDF for $\lambda = 27.5°$

Figure 3.9: Probability density functions of the separation shock movement extracted from the PSP images for both ramps. The black lines represent a Gaussian distribution.

Approved for Public Release; Distribution Unlimited. Case Number AFRL-2024-5997; Cleared 10/25/2024.



(a) PSD for $\lambda = 10°$.



(b) PSD for $\lambda = 27.5°$.

Figure 3.10: Pre-multiplied power spectral densities of the separation shock foot motion for both ramps. Zero-crossing frequencies and Strouhal numbers based on boundary layer thickness and intermittent length scale are shown.

Chapter 4

Conclusions and Future Work

4.1 Conclusions

Experiments have been conducted to characterize the dynamics of three swept compression ramps with sweep angles of $\lambda = 0°$, $\lambda = 10°$, and $\lambda = 27.5°$ subjected to Mach 4 flow. Data were collected using oil flow visualization, fast-response pressure sensitive paint (PSP), and unsteady pressure transducers in UTSI's Mach 4 Ludwieg Tube. Data for the $\lambda = 0°$ were unable to be processed as a result of data loss due to hard drive malfunction and damage to the unswept ramp during subsequent experiments. The remaining data show clear differences in the shape of the separation regions when comparing the low sweep and high sweep ramps. The ramp with low sweep exhibited cylindrical symmetry (i.e., the separation and reattachment lines are parallel), whereas the highly-swept ramp showed quasi-conical symmetry (i.e., the separation and reattachment lines diverge in the spanwise direction).

Interestingly, the data indicate that, along the centerline, the separation shock is closer to the ramp corner for the more highly-swept ramp. This was noted in both the oil flow visualization and unsteady pressure sensitive paint. The current effort is part of a larger study within which similar configurations were tested by Allen *et al.* [2] in Mach 2 freestream conditions. They observed the opposite trend in regards to the separation shock location and the sweep angle. Although this discrepancy is likely due to the difference in physical scale, as the separation region length appears to be more dependent on the distance from the virtual conical origin than the inviscid shock strength.

The unsteadiness in the surface pressures were calculated and seen to be higher in the observable region of interest in the low sweep case compared to the high sweep case.

Approved for Public Release; Distribution Unlimited. Case Number AFRL-2024-5997; Cleared 10/25/2024.

The reattachment region has pressure fluctuations that are approximately three times greater than those in the separation region for both sweep angles. The high sweep case compares favorably to similar swept ramp experiments conducted by Erengil and Dolling [12], indicating that the normalized surface pressure fluctuations may not be strongly dependent on certain geometric parameters. An empirical relationship may exist between the normalized surface pressure fluctuations and the shock strength in terms of Mach number, compression angle, and sweep angle, although more experimentation would be required to address this hypothesis.

Separation shock foot motion extracted from the unsteady PSP experiments allowed for further analysis of the unsteadiness in the separation region. In both the low and high sweep cases, the separation shock motion possesses a normal distribution. However, the spectral content for the low sweep case showed that elevated unsteadiness may be present in the range of 200–400 Hz. In contrast, the high sweep case showed more dominant spectral content within the range of 700–800 Hz. In both cases, however, the Strouhal number based on the intermittent length scales fell within the typical range of $0.02 \leq St_L \leq 0.05$ for turbulent SBLIs as reported in previous literature from Clemens and Narayanaswamy [7] and Dussauge *et al.* [10].

4.2 Future Work

As outlined by Clemens and Narayanaswamy [7], there are ongoing discussions within academia regarding the drivers of unsteadiness in SBLIs. One prevailing theory is that the upstream mechanism (i.e., the incoming boundary layer) primarily influences the unsteadiness. Another theory is that the downstream mechanism (i.e., the subsonic flow in the separated region) allows information to propagate upstream and drive the unsteadiness in the SBLI. In reality, both mechanisms are likely coupled to form the complex dynamics of SBLIs. Regardless, the incoming boundary-layer profile and subsonic extent of the separation region play an important role in driving the unsteadiness in these interactions.

The original scope of this work included MTV experiments to measure the incoming boundary-layer velocity profile, but were canceled due to component failure within the

Approved for Public Release; Distribution Unlimited. Case Number AFRL-2024-5997; Cleared 10/25/2024.

laser. The lack of velocity data for this particular experiment make it difficult to address both the incoming boundary-layer profile and subsonic extent of the separation region. Further experimentation using MTV or Particle Image Velocimetry (PIV) on the geometries presented here would be extremely helpful in determining unsteadiness drivers. At the time of this writing, UTSI is in the process of constructing a Mach 3.5 blowdown facility of the same test section dimensions as the Mach 2 facility used by Allen [2]. A continuation of their experiments using the same models at higher Mach number would be useful in rounding out UTSI's portfolio of swept compression ramp work at varying compression angle, sweep angle, Mach number, and Reynolds number.

Approved for Public Release; Distribution Unlimited. Case Number AFRL-2024-5997; Cleared 10/25/2024.

Bibliography

[1] (2022). *Porous, Fast-Response Pressure Sensitive Paint.* Innovative Scientific Solutions, Inc. 23

[2] Allen, D. S., Langley, K. R., Schmisseur, J. D., and Kreth, P. A. (2023). Separation region unsteadiness drivers in swept compression ramps. In *AIAA SCITECH 2023 Forum*, page 2490. 5, 6, 22, 34, 42, 49, 51

[3] Asai, K., Kanda, H., Cunningham, C. T., Erausquin, R., and Sullivan, J. P. (1997). Surface pressure measurement in a cryogenic wind tunnel by using luminescent coating. In *ICIASF'97 Record. International Congress on Instrumentation in Aerospace Simulation Facilities*, pages 105–114. IEEE.

[4] Asai, K., Nakakita, K., Kameda, M., and Teduka, K. (2001). Recent topics in fast-responding pressure-sensitive paint technology at national aerospace laboratory. In *ICIASF 2001 Record, 19th International Congress on Instrumentation in Aerospace Simulation Facilities (Cat. No. 01CH37215)*, pages 25–36. IEEE.

[5] Baron, A. E., Danielson, J., Gouterman, M., Wan, J. R., Callis, J. B., and McLachlan, B. (1993). Submillisecond response times of oxygen-quenched luminescent coatings. *Review of Scientific Instruments*, 64(12):3394–3402. 18

[6] Butera, J. G., Smith, C. D., and Schmisseur, J. D. (2023). Hypersonic ground tests of bolt ii using optical diagnostics. In *AIAA SCITECH 2023 Forum*, page 1190. 22

[7] Clemens, N. T. and Narayanaswamy, V. (2014). Low-frequency unsteadiness of shock wave/turbulent boundary layer interactions. *Annual Review of Fluid Mechanics*, 46:469–492. 2, 44, 50

Approved for Public Release; Distribution Unlimited. Case Number AFRL-2024-5997; Cleared 10/25/2024.

[8] Crafton, J. W., Stanfield, S., Rogoshchenkov, N., and Schmit, R. F. (2017). Investigation of passive flow control of cavity acoustics using dynamic pressure-sensitive paint. In *55th AIAA Aerospace Sciences Meeting*, page 1178. 18

[9] Dolling, D. S. (2001). Fifty years of shock-wave/boundary-layer interaction research: what next? *AIAA journal*, 39(8):1517–1531. 1

[10] Dussauge, J.-P., Dupont, P., and Debiéve, J.-F. (2006). Unsteadiness in shock wave boundary layer interactions with separation. *Aerospace Science and Technology*, 10(2):85–91. 44, 50

[11] Eagan, G. D., Lewis, C. J., Alles, R. M., Klingaman, K. C., Davenport, K., Gragston, M. T., Rice, B. E., Hamilton, M. C., and Thurow, B. S. (2023). Direct measurements of shock impingement in a busemann inlet via a miniature embedded imaging system. In *AIAA SCITECH 2023 Forum*, page 2256. 13

[12] Erengil, M. and Dolling, D. (1993). Effects of sweepback on unsteady separation in mach 5 compression ramp interactions. *AIAA Journal*, 31(2):302–311. ix, 3, 38, 42, 43, 44, 46, 50

[13] Fujii, S., Numata, D., Nagai, H., and Asai, K. (2013). Development of ultrafast-response anodized-aluminum pressure-sensitive paints. In *51st AIAA Aerospace Sciences Meeting Including the New Horizons Forum and Aerospace Exposition*, page 485.

[14] Furuya, T., Nakai, T., Imai, M., and Kameda, M. (2021). Characterization and improvement of heat resistance of a polymer-ceramic pressure-sensitive paint at high temperatures. *Sensors*, 21(24):8177.

[15] Gaitonde, D. V. (2015). Progress in shock-wave/boundary-layer interactions. *Progress in Aerospace Sciences*, 72:80–99. 1

[16] Gaitonde, D. V. and Adler, M. C. (2023). Dynamics of three-dimensional shock-wave/boundary-layer interactions. *Annual Review of Fluid Mechanics*, 55:291–321. 2

Approved for Public Release; Distribution Unlimited. Case Number AFRL-2024-5997; Cleared 10/25/2024.

[17] Gongora-Orozco, N., Zare-Behtash, H., and Kontis, K. (2010). Global unsteady pressure-sensitive paint measurements of a moving shock wave using thin-layer chromatography. *Measurement*, 43(1):152–155.

[18] Gouterman, M. (1997). Oxygen quenching of luminescence of pressure sensitive paint for wind tunnel research. 21

[19] Gragston, M. and Smith, C. D. (2022). 10 khz molecular tagging velocimetry in a mach 4 air flow with acetone vapor seeding. *Experiments in Fluids*, 63(5):85. 26

[20] Gregory, J. (2004). Porous pressure-sensitive paint for measurement of unsteady pressures in turbomachinery. In *42nd AIAA Aerospace Sciences Meeting and Exhibit*, page 294.

[21] Gregory, J., Asai, A., Kamada, M., Liu, T., and Sullivan, J. (2008). A review of pressure sensitive paints in hypersonic and unsteady flows. *Journal of Aerospace Engineering*, 222(2):249–290.

[22] Gregory, J. W. (2002). Unsteady pressure measurements in a turbocharger compressor using porous pressure-sensitive paint. *MS Thesis, School of Aeronautics and Astronautics, Purdue University*.

[23] Gregory, J. W., Sakaue, H., Liu, T., and Sullivan, J. P. (2014). Fast pressure-sensitive paint for flow and acoustic diagnostics. *Annual Review of Fluid Mechanics*, 46:303–330. viii, 19

[24] Gregory, J. W. and Sullivan, J. P. (2006). Effect of quenching kinetics on unsteady response of pressure-sensitive paint. *AIAA journal*, 44(3):634–645.

[25] Hangai, T., Kameda, M., Nakakita, K., and Asai, K. (2002). Time response characteristics of pyrene-based pressure-sensitive coatings on anodic porous alumina. In *Proceedings of the 10th International Symposium on Flow Visualization, Kyoto, Japan*, pages 26–29.

Approved for Public Release; Distribution Unlimited. Case Number AFRL-2024-5997; Cleared 10/25/2024.

[26] Kameda, M., Tezuka, N., Hangai, T., Asai, K., Nakakita, K., and Amao, Y. (2004). Adsorptive pressure-sensitive coatings on porous anodized aluminium. *Measurement Science and Technology*, 15(3):489.

[27] Kavandi, J. (1990). Luminescense imaging for aerodynamic pressure measurements. viii, 20

[28] Kavandi, J., Callis, J., Gouterman, M., Khalil, G., Wright, D., Green, E., Burns, D., and McLachlan, B. (1990). Luminescent barometry in wind tunnels. *Review of Scientific Instruments*, 61(11):3340–3347. 17

[29] Kline, S. J. and McClintock, F. A. (1963). Describing uncertainties in single-sample experiments. *Mechanical Engineering*, 75:3–8. 29

[30] Knight, D., Yan, H., Panaras, A. G., and Zheltovodov, A. (2003). Advances in cfd prediction of shock wave turbulent boundary layer interactions. *Progress in Aerospace Sciences*, 39(2-3):121–184. 2

[31] Knight, D. D., Horstman, C., and Bogdonoff, S. (1992). Structure of supersonic turbulent flow past a swept compression corner. *AIAA Journal*, 30(4):890–896.

[32] Korkegi, R. H. (1975). Comparison of shock-induced two-and three-dimensional incipient turbulent separation. *AIAA Journal*, 13:534–535. 11

[33] Kreth, P. A., Gragston, M., Davenport, K., and Schmisseur, J. D. (2021). Design and initial characterization of the utsi mach 4 ludwieg tube. In *AIAA Scitech 2021 Forum*, page 0384. viii, 9, 10

[34] Ledbetter, S. Y., Lester, L. E., Garner, A. N., Goldston, H. R., Smith, C. D., Gragston, M., Kreth, P. A., and Schmisseur, J. D. (2023). Analysis of streamwise vortex streaks in shockwave-boundary layer interactions on a hollow cylinder-flare at m = 4. In *AIAA AVIATION 2023 Forum*, page 3698. 22

[35] Liu, T., Bencic, T., and Sullivan, J. (1999). Pressure sensitive paints. *submitted for Experiments in Fluids*. 17

[36] Liu, T., Campbell, B. T., Burns, S. P., Sullivan, J. P., et al. (1997). Temperature- and pressure-sensitive luminescent paints in aerodynamics. *Applied Mechanics Reviews*, 50:227–246. 17, 21

[37] Lu, F. (2010). Surface oil flow visualization: Still useful after all these years. *The European Physical Journal Special Topics*, 182(1):51–63. 13

[38] Masuda, T., Isobe, E., Higashimura, T., and Takada, K. (1983). Poly [1-(trimethylsilyl)-1-propyne]: a new high polymer synthesized with transition-metal catalysts and characterized by extremely high gas permeability. *Journal of the American Chemical Society*, 105(25):7473–7474.

[39] McLachlan, B. G. and Bell, J. H. (1995). Pressure-sensitive paint in aerodynamic testing. *Experimental thermal and fluid science*, 10(4):470–485. 17

[40] Mosharov, V., Radchenko, V., and Fonov, S. (1997). Luminescent pressure sensors in aerodynamic experiment, moscow: Cent. *Aerohydrodynamic Inst.(TsAGI). CWA International Corp*, 151.

[41] Murakami, D. D., Shaw-Lecerf, M., Lash, E. L., Lyons, K., and Roozeboom, N. (2023). Implementation of the lifetime method in unsteady pressure-sensitive paint measurements. In *AIAA SCITECH 2023 Forum*, page 0635. 22

[42] Pandey, A. and Gregory, J. W. (2016). Frequency-response characteristics of polymer/ceramic pressure-sensitive paint. *AIAA Journal*, 54(1):1.

[43] Peng, D., Jensen, C. D., Juliano, T. J., Gregory, J. W., Crafton, J., Palluconi, S., and Liu, T. (2013). Temperature-compensated fast pressure-sensitive paint. *AIAA journal*, 51(10):2420–2431. 18

[44] Peng, D. and Liu, Y. (2020). Fast pressure-sensitive paint for understanding complex flows: from regular to harsh environments. *Experiments in Fluids*, 61(1):1–22.

[45] Peterson, J. I. and Fitzgerald, R. V. (1980). New technique of surface flow visualization based on oxygen quenching of fluorescence. *Review of Scientific Instruments*, 51(5):670–671. 17

[46] Pitz, R. W. and Danehy, P. M. (2023). *Molecular Tagging Velocimetry in Gases*, pages 539–588. American Institute of Aeronautics and Astronautics, Reston, VA. 25

[47] Ponomarev, S. and Gouterman, M. (1998). Fast responding pressure sensitive paints based on high concentration of hard particles in polymer. In *Proceedings of the 6th Annual Pressure-Sensitive Paint Workshop, The Boeing Co., Seattle, WA*, pages 31–1. 18

[48] Puklin, E., Carlson, B., Gouin, S., Costin, C., Green, E., Ponomarev, S., Tanji, H., and Gouterman, M. (2000). Ideality of pressure-sensitive paint. i. platinum tetra (pentafluorophenyl) porphine in fluoroacrylic polymer. *Journal of Applied Polymer Science*, 77(13):2795–2804.

[49] Roozeboom, N., Baerny, J. K., Murakami, D. D., Ngo, C., and Powell, J. M. (2020). Recent developments in nasa's unsteady pressure-sensitive paint capability. In *AIAA Scitech 2020 Forum*, page 0516. 22

[50] Roozeboom, N., Powell, J., Baerny, J., Murakami, D., Ngo, C., Garbeff, T. J., Ross, J. C., and Flach, R. (2019). Development of unsteady pressure-sensitive paint application on nasa space launch system. In *AIAA Aviation 2019 Forum*, page 3502. 22

[51] Sakaue, H., Morita, K., Iijima, Y., and Sakamura, Y. (2013). Response time scales of anodized-aluminum pressure-sensitive paints. *Sensors and Actuators A: Physical*, 199:74–79.

[52] Sakaue, H. and Sullivan, J. P. (2001). Time response of anodized aluminum pressure-sensitive paint. *AIAA journal*, 39(10):1944–1949.

[53] Sakaue, H., Sullivan, J. P., Asai, K., Iijima, Y., and Kunimasu, T. (1999). Anodized aluminum pressure sensitive paint in a cryogenic wind tunnel. In *Instrumentation in the Aerospace Industry: Proceedings of the International Symposium*, pages 337–346.

[54] Scroggin, A., Slamovich, E., Crafton, J., Lachendro, N., and Sullivan, J. (1999). Porous polymer/ceramic composites for luminescence-based temperature and pressure measurement. *MRS Online Proceedings Library (OPL)*, 560.

[55] Settles, G. S. and Teng, H.-Y. (1984). Cylindrical and conical flow regimes of three-dimensional shock/boundary layer interactions. *AIAA Journal*, 22(2):194–200. viii, 2, 3, 7

[56] Shoppell, Z. M. (2023). An experimental investigation of the effect of narrowband freestream noise on fundamental transitional shockwave-boundary layer interaction mechanisms.

[57] Siddiqui, F. and Gragston, M. (2023). Multi-point fleet velocimetry in a mach 4 ludwieg tuble using a diffractive optical element. 26

[58] Sun, C.-C. and Childs, M. E. (1973). A modified wall wake velocity profile for turbulent compressible boundary layers. *Journal of Aircraft*, 10(6):381–383.

[59] Vanstone, L. and Clemens, N. T. (2019). Unsteadiness mechanisms of a swept compression-ramp shock/boundary layer interactions at mach 2. In *AIAA Scitech 2019 Forum*, page 0095. 4

[60] Vanstone, L., Goller, T., Mears, L., and Clemens, N. T. (2019). Separated flow unsteadiness in a mach 2 swept compression-ramp interaction using high-speed psp. In *AIAA Aviation 2019 Forum*, page 3645. 43, 44

[61] Vanstone, L., Saleem, M., Seckin, S., and Clemens, N. T. (2015). Experimental investigation of unsteadiness of swept-ramp shock/boundary layer interactions at mach 2. In *45th AIAA Fluid Dynamics Conference*, page 2932. 4

[62] Vanstone, L., Saleem, M., Seckin, S., and Clemens, N. T. (2016). Effect of upstream boundary layer on unsteadiness of swept-ramp shock/boundary layer interactions at mach 2. In *54th AIAA Aerospace Sciences Meeting*, page 0076. 4

[63] Vanstone, L., Saleem, M., Seckin, S., and Clemens, N. T. (2018). Experimental study of the mean structure and quasi-conical scaling of a swept-compression-ramp interaction at mach 2. *Journal of Fluid Mechanics*, pages 1–27. 4

Approved for Public Release; Distribution Unlimited. Case Number AFRL-2024-5997; Cleared 10/25/2024.

[64] Watts, J. D. (1968). Flight experience with shock impingement and interference heating on the x-15-2 research airplane. *NASA TM X-1669*. 1

[65] Wheeler, A. J. and Ganji, A. R. (1996). *Introduction to Engineering Experimentation*, volume 199. Prentice Hall New Jersey. 29

[66] Woike, M. R., Davis, D. O., Clem, M. M., and Crafton, J. (2017). The investigation of shock wave boundary layer interactions using fast pressure sensitive paint and surface stress sensitive film measurement techniques. In *33rd AIAA Aerodynamic Measurement Technology and Ground Testing Conference*, page 3732. 18

Approved for Public Release; Distribution Unlimited. Case Number AFRL-2024-5997; Cleared 10/25/2024.

Appendix

A Use of Figures from Published Works

A.1 Figure 1.1

Per the American Institute of Aeronautics and Astronautics (AIAA) website, figures are allowed to be reproduced from AIAA documents with permission from the copyright holder. In the case of this figure, AIAA is the copyright holder, and the correct permissions were obtained via the Copyright Clearance Center (CCC) as outlined by AIAA.

A.2 Figure 2.5

Per the Annual Review of Fluid Mechanics website, all requests for permission for use of content are referred to the Copyright Clearance Center (CCC). Correct permissions were obtained via the CCC.

Approved for Public Release; Distribution Unlimited. Case Number AFRL-2024-5997; Cleared 10/25/2024.

Vita

Jamison Murphree is a native of McEwen, Tennessee who completed his Bachelor's degree in Aerospace Engineering at the University of Tennessee, Knoxville in May 2022. Following graduation, Jamison began work on his Master's degree in Aerospace Engineering at the University of Tennessee Space Institute. He worked with the HORIZON research group as a Graduate Research Assistant studying high-speed flow phenomena and optical diagnostic techniques. Jamison is an active member of the American Institute of Aeronautics and Astronautics (AIAA) and the University Consortium for Applied Hypersonics (UCAH). Following the completion of his Master's degree, Jamison plans to continue work in the aerospace industry as a test engineer for the U.S. Government or related contractors.

Approved for Public Release; Distribution Unlimited. Case Number AFRL-2024-5997; Cleared 10/25/2024.